Published in final edited form as:

Mol Cell. 2022 March 03; 82(5): 950–968.e14. doi:10.1016/j.molcel.2022.02.011.

Regulation of GTPase function by autophosphorylation

Christian W. Johnson[1,2], **Hyuk-Soo Seo**[1,3], **Elizabeth M. Terrell**[4], **Moon-Hee Yang**[1,2], **Fenneke KleinJan**[5], **Teklab Gebregiworgis**[5], **Genevieve M.C. Gasmi-Seabrook**[5], **Ezekiel A. Geffken**[1], **Jimit Lakhani**[1], **Kijun Song**[1], **Puspalata Bashyal**[1], **Olesja Popow**[1,2,6], **Joao A. Paulo**[6], **Andrea Liu**[1], **Carla Mattos**[7], **Christopher B. Marshall**[5], **Mitsuhiko Ikura**[5], **Deborah K. Morrison**[4], **Sirano Dhe-Paganon**[1,3], **Kevin M. Haigis**[1,2,8,*]

[1]Department of Cancer Biology, Dana-Farber Cancer Institute, Boston, MA 02215, USA

[2]Department of Medicine, Brigham & Women's Hospital and Harvard Medical School, Boston, MA 02115, USA

[3]Department of Biological Chemistry & Molecular Pharmacology, Harvard Medical School, Boston, MA 02115, USA

[4]Laboratory of Cell and Developmental Signaling, NCI-Frederick, Frederick, MD 21702, USA

[5]Princess Margaret Cancer Centre, University Health Network, Toronto, ON M5G 1L7, Canada

[6]Department of Cell Biology, Harvard Medical School, Boston, MA 02115, USA

[7]Department of Chemistry and Chemical Biology, Northeastern University, Boston, MA 02115, USA

[8]Lead contact

SUMMARY

A unifying feature of the RAS superfamily is a conserved GTPase cycle by which these proteins transition between active and inactive states. We demonstrate that autophosphorylation of some GTPases is an intrinsic regulatory mechanism that reduces nucleotide hydrolysis and enhances nucleotide exchange, altering the on/off switch that forms the basis for their signaling functions. Using X-ray crystallography, nuclear magnetic resonance spectroscopy, binding assays, and molecular dynamics on autophosphorylated mutants of H-RAS and K-RAS, we show that phosphoryl transfer from GTP requires dynamic movement of the switch II

*Correspondence: Kevin_Haigis@dfci.harvard.edu.

AUTHOR CONTRIBUTIONS

C.W.J. and K.M.H. conceived and drafted the overall paper. C.M. and C.W.J. were responsible for crystallization studies of H-RAS^{A59T} and H-RAS^{A59E}. H.-S.S., E.A.G., J.L., K.S., P.B., and S.D.-P. were responsible for crystallization of K-RAS^{A59E} and preparing protein for intact mass spectrometry. M.-H.Y. performed signaling studies on mouse embryonic stem cells and validation of autophosphorylation of fast-exchange mutants with the A59T mutation in cells. E.M.T. and D.K.M. designed the BRET and co-immunoprecipitation experiments and interpreted the data. E.M.T. performed BRET and co-immunoprecipitation assays. O.P. and J.A.P. were responsible for mass spectrometry experiments validating autophosphorylation. NMR and Biolayer interferometry experiments were done by F.K., T.G., G.M.C.G.-S., C.B.M., and M.I. A.L. helped with creation of Table 1. C.W.J. performed all other experiments.

DECLARATION OF INTERESTS

K.M.H. is married to a member of *Molecular Cell*'s Advisory Board.

SUPPLEMENTAL INFORMATION

Supplemental information can be found online at https://doi.org/10.1016/j.molcel.2022.02.011.

region and that autophosphorylation promotes nucleotide exchange by opening the active site and extracting the stabilizing Mg^{2+}. Finally, we demonstrate that autophosphorylated K-RAS exhibits altered effector interactions, including a reduced affinity for RAF proteins in mammalian cells. Thus, autophosphorylation leads to altered active site dynamics and effector interaction properties, creating a pool of GTPases that are functionally distinct from their non-phosphorylated counterparts.

In brief

Johnson et al. identify a group of GTPases that undergo autophosphorylation via a conserved active site substitution. Using RAS^{A59T} as a prototypical autophosphorylating GTPase, they show that autophosphorylation is a stable post-translational modification that inhibits GTP hydrolysis and enhances nucleotide exchange. Despite promoting cell transformation, autophosphorylation inhibits K-RAS effector interactions.

Graphical Abstract

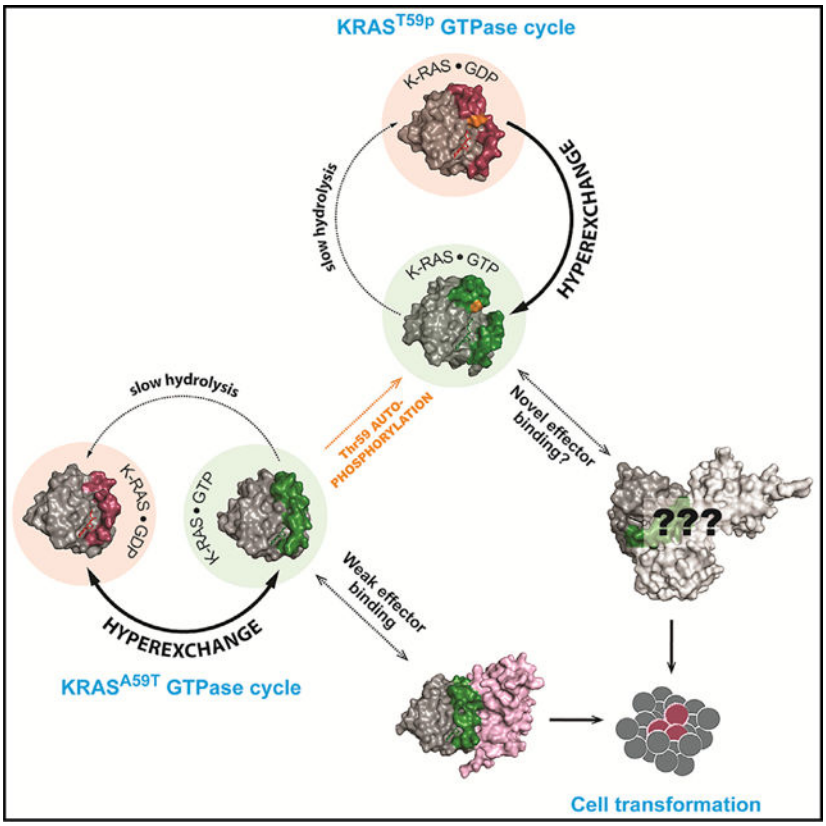

INTRODUCTION

Proteins of the RAS GTPase superfamily coordinate cellular behaviors in response to extracellular signals. The current paradigm is that these signaling hubs are inactive when bound to guanine nucleotide diphosphate (GDP) and active when bound to guanine nucleotide triphosphate (GTP), with cycling between these states regulated by

intrinsic mechanisms of GTP hydrolysis and nucleotide exchange or by mechanisms facilitated by GTPase activating proteins (GAPs) and guanine nucleotide exchange proteins (GEFs) (Cherfils and Zeghouf, 2013). When bound to GTP, the active sites of GTPases undergo conformational changes that allow interaction and activation of effector proteins. Furthermore, GTPases undergo a number of post-translational modifications (PTMs) that regulate their dynamics, subcellular localization, and activity. Dysregulation of the GTPase cycle by mutations in either GTPases or their regulators can lead to cancer, neurological diseases, or developmental syndromes (Qu et al., 2019; Simanshu et al., 2017). While this aspect of GTPases is well studied, there is less known about how pathogenic mutations and PTMs interact to modulate the function of GTPases.

Much of what we know about the core biochemical properties of GTPases comes from early studies of oncogenic RAS encoded by the Harvey and Kirsten RAS tumor viruses. Intriguingly, while the viral proteins exhibit a high degree of sequence identity with their cellular homologs, substitution of alanine at amino acid 59 for threonine (A59T) is the only shared difference, suggesting that the change in biochemical function resulting from this substitution provides a selective advantage for viral tumorigenesis. The Thr59 substitution is buried in the active site of RAS and undergoes autophosphorylation when RAS is bound to GTP (Shih et al., 1980). For this reason, H-RAS was initially thought to be a serine/threonine kinase. We now know that the primary biochemical activity of cellular RAS proteins is GTP hydrolysis, which is defective in the viral oncoproteins mutations at codon 12 (G12R in v-H-RAS and G12S in v-K-RAS).

The biological advantage of Thr59 in v-RAS, and the relevance of its associated phosphorylation, is still not understood. Most members of the small GTPase superfamily have alanine at residue 59, however, a small number of family members carry an autophosphorylation motif at this position (Table 1). In some of these, autophosphorylation has been observed, including H-RAS (Chung et al., 1993), RALA (Frech et al., 1990), RAB1B (Touchot et al., 1989), and elongation factor Tu (Cool et al., 1990). Thus, autophosphorylation appears to be possible when either a threonine or serine nucleophile is present in the active site at this position, suggesting that autophosphorylation is a conserved enzymatic function in small GTPases.

Substitutions at Ala59 of K-, H-, and N-RAS—including threonine (A59T) and glutamate (A59E) substitutions—represent approximately 0.2% of oncogenic RAS mutations, implicating autophosphorylation in RAS oncogenicity, yet the molecular and cellular properties of these mutants are poorly characterized (Haigis, 2017). In this study, we sought to understand how autophosphorylation changes H- and K-RAS function. Furthermore, our studies suggest that other small GTPases with an autophosphorylation motif share this unique mechanism of activation.

RESULTS

Autophosphorylation alters the GTPase cycle of K-RAS

In a colon cancer cell line carrying endogenous K-RAS^{A59T} (SNU-175), we noted that K-RAS protein exhibited an electrophoretic shift (Figure 1A), as did purified protein expressed

in *E. coli* (Figure 1B). We confirmed by mass spectroscopy of purified protein that Thr59 was phosphorylated, indicating that phosphorylation is an intrinsic property of K-RAS^{A59T} (Figures S1A and S1B), and subsequently showed in two ways that autophosphorylation resulted in the electrophoretic shift. First, K-RAS^{A59E}—a phosphomimetic substitution—migrated at a similar speed as the upper K-RAS^{A59T} band (Figure 1B). Second, the upper K-RAS^{A59T} band could be removed by lambda phosphatase treatment, albeit inefficiently and only after the protein was denatured (Figure 1C). This was an important observation because it suggested that phosphorylated Thr59 is protected by the tertiary structure of K-RAS. Using the electrophoretic shift as a readout, we measured the kinetics of autophosphorylation of purified K-RAS^{A59T} (Figures 1D and S1C), which produced results similar to historical studies on H-RAS^{A59T}, affirming that autophosphorylation occurs via an intramolecular reaction (John et al., 1988).

The relationship between GTP hydrolysis and autophosphorylation is not defined. One possibility is that RAS autophosphorylation is a passive byproduct of the hydrolysis reaction and that Thr59 acts as a nucleophile that substitutes for the catalytic water present in the active site. If this were true, we would expect GAP, which binds to RAS proteins and enhances hydrolysis, to likewise enhance the rate of autophosphorylation. To the contrary, we found that autophosphorylation was not enhanced by GAP (Figures 1D and S1C; Table S1). Thus, autophosphorylation is not a byproduct of hydrolysis, but is sensitive to active site conformation and is mechanistically independent of GTP hydrolysis. Furthermore, enhancement of nucleotide exchange by addition of SOS1 did not significantly affect the rate of autophosphorylation (Figures 1D and S1C; Table S1). Because active site dynamics of K-RAS are modulated by growth signals received by cells, we tested whether the levels of autophosphorylated K-RAS^{A59T} (K-RAS^{A59Tp}) changed in response to epidermal growth factor (EGF) or insulin stimulation (Figures 1E and S1D; Table S1). We observed no changes in the relative amount of K-RAS^{A59Tp} in these experiments, suggesting that autophosphorylation is not dynamically regulated by upstream signals.

A59T and A59E are cancer-associated mutations of RAS. Because cancer-associated mutations hyperactivate RAS proteins by altering the GTPase cycle, we examined how mutation and/or Thr59 phosphorylation affect cycling. We found that residue 59 mutants of K-RAS exhibited impaired intrinsic and GAP-mediated GTP hydrolysis, like the strongly activated mutant K-RAS^{G12D} (Figure 1F and Table S1). The effects on nucleotide exchange were more complex (Figures 1G, S1E, and S1F; Table S1). First, mutation and phosphorylation strongly enhanced the rate of intrinsic exchange. Second, K-RAS^{A59T} remained sensitive to GEF-induced exchange, while K-RAS^{A59Tp} was less sensitive and K-RAS^{A59E} was entirely resistant. Third, while K-RAS$^{A59T/E}$ showed no preference for GDP or GTP exchange, K-RAS^{A59Tp} preferentially exchanged GDP for GTP.

Our experiments demonstrate that K-RAS^{A59Tp} and K-RAS^{A59E} have a significant impact on the dynamics of nucleotide exchange and hydrolysis, which leads to functional activation by increasing the steady-state levels of GTP-bound K-RAS. We noted that many of the GTPases in Table 1 share the biochemical characteristics of residue 59 mutants, including high rates of nucleotide exchange coupled with low rates of GTP hydrolysis and dominance of the active GTP-bound state. Furthermore, mutation of Ser64 of RhoE/RND3 to alanine

rescues GTP hydrolysis and limits intrinsic nucleotide exchange of this GTPase (Foster et al., 1996). Altogether, these observations indicate that autophosphorylation may be a normal regulatory function of these GTPases.

Switch II mobility promotes autophosphorylation

Our data suggest that the mechanism of autophosphorylation is not a byproduct of GTP hydrolysis. A previous crystal structure of H-RAS$^{G12V/A59T}$ (PDB: 521P) shows an active site unfavorable for autophosphorylation because Thr59 is oriented away from GTP (Figure S2A) (Krengel et al., 1990). To help explain the mechanism of phosphorylation, we solved two crystal structures of H-RAS^{A59T} bound to a non-hydrolyzable GTP analog (GppNHp) (Figure S2B and Table 2). We chose H-RAS because it favors a closed active site, while K-RAS favors an open active site (Johnson et al., 2019; Parker et al., 2018). We reasoned that active site closure was necessary for γ-phosphate de-solvation to favor phosphoryl transfer to Thr59. Our crystal structures revealed that the A59T mutation disconnects switch II from both the switch I and the P loop and, in agreement with the observed reduction in GTP hydrolysis, displaces the nucleophilic water out of the active site (Figures 2A and S2C). Thr59 rearranges the active site through a clash between its methyl group and Tyr64 while its hydroxyl group forms optimal H-bonds with the backbone of Thr35 and Gln61 (black bonds (1) in Figure 2A). This results in switch II shifting away from the active site (black and gray bonds (2) in Figure 2A) and breaking the H-bond between Gly60 and Gly12 in the P loop (gray bonds (3) in Figure 2A) that normally stabilizes active site closure upon GTP binding. Next, the Thr35-Thr59 interaction breaks the β sheet H-bond between Thr58 and Ile36, causing destabilization of switch I. The β sheet Thr58-Ile36 interaction is characteristic of wild-type H-RAS, but is absent in other fast-exchange mutants of RAS (Johnson et al., 2019).

Our H-RAS^{A59T} structures suggest that movement of Thr59 toward the γ-phosphate of GTP, a necessary step for autophosphorylation, is possible (Figure S2D). Comparison of available crystal structures of GTP-bound small GTPases showed similar orientations and distances between their corresponding residue and the γ-phosphate, supporting their potential to undergo autophosphorylation (Figures 2B and S2E). Likewise, purified K-RAS^{A59S}, K-RAS^{A59H}, and K-RAS^{A59Y} proteins demonstrate a weak capacity to undergo autophosphorylation under the same reaction conditions as K-RAS^{A59T} (Figure S2F). Nevertheless, it was unclear how residue 59 reaches the γ-phosphate. To answer this question, we used molecular dynamics (MD) simulations to monitor active site motions in K-RAS^{A59T} and other GTPases. Throughout the K-RAS^{A59T} simulation, Thr59 closely associated with the γ-phosphate of GTP while maintaining its interaction with Gln61 (Figure 2C). In contrast, the Thr35-Thr59 interaction was commensurate with Thr59 pulling away from GTP and Q61 in switch II (Figure 2C). Consistently, simulations with the other GTPases showed strong association of residue 59 with GTP that was regulated by residue 35 in switch I (Figures 2D and S2G).

Gly12 co-mutations can enhance the steady-state phosphorylation of H-RAS^{A59T} in NIH 3T3 cells by enhancing the rate of autophosphorylation (Gibbs et al., 1984). We tested the potentially competitive nature of the Thr59-Thr35 interaction with autophosphorylation by

examining the ratio of phosphorylated protein in the presence of different co-mutations. We found that K-RAS$^{G12V/A59T}$, and the fast-exchange mutations (i.e., K-RAS$^{G13D/A59T}$ and K-RAS$^{A59T/A146T}$), increased autophosphorylation relative to K-RAS^{A59T} and K-RAS$^{G12R/A59T}$ (Figure S2H). These results are consistent with a role for switch I in dictating autophosphorylation because these mutants favor opening of the active site (Johnson et al., 2019; Poulin et al., 2019). In contrast, Arg12 directly interacts with switch II in crystal structures of K-RAS^{G12R}, which suggests that in K-RAS$^{G12R/A59T}$, movement of Thr59 toward the γ-phosphate is unfavourable (Hobbs et al., 2020).

Our MD analysis validates that serine and/or threonine nucleophiles in the proper active site position are poised for phosphoryl transfer after switch II movement toward the γ-phosphate (Figure 2E). The simple mechanism presented in Figure 2E is consistent with the observed effect on K-RAS autophosphorylation by GAP and SOS1. GAP makes significant interactions with switch II, essentially locking it into a particular conformation for duration of the complex and preventing movement of Thr59 to GTP (Figure 1D). Likewise, while the crystal structure of H-RAS bound to SOS1 shows that the catalytic domain of SOS1 would move Thr59 toward GTP (Boriack-Sjodin et al., 1998), which is a major determinant of autophosphorylation rate (Chung et al., 1993), our data suggest that the hydroxyl nucleophile of Thr59 is activated and carefully oriented by intramolecular interactions with switch II.

A "Mg^{2+} extraction" mechanism for hyperexchange

We next addressed how alterations at position 59 promote high rates of nucleotide exchange (hyperexchange) and why K-RAS^{A59Tp} and K-RAS^{A59E} have exchange properties that are different from K-RAS^{A59T}. First, we explored the dynamics of GDP-bound K-RAS^{A59T} and K-RAS^{A59E} using ^{1}H-^{15}N heteronuclear single quantum coherence (HSQC) nuclear magnetic resonance (NMR) spectroscopy in reference to wild-type K-RAS (Figure 3A). Consistent with our nucleotide exchange data, we observed chemical shift perturbation in backbone amide protons around the active sites of both K-RAS^{A59T} and K-RAS^{A59E}. Overall, Glu59 displayed a more global effect on K-RAS backbone chemical shifts than Thr59, indicating a more significant effect on K-RAS tertiary structure. Notably, while the switch I region (residues 28–40) showed the largest chemical shift changes in K-RAS^{A59T}, the same region experienced further peak broadening in K-RAS^{A59E}, suggesting that a conformational coupling between Thr59 and the active site in switch I is enhanced by Glu59 substitution. These chemical shift changes are consistent with Thr59 motions and associated local changes around this residue in switch II, and are consistent with our crystal structures and MD simulations.

To better understand the structural changes induced by autophosphorylation and the chemical shift perturbations seen in K-RAS^{A59E}, we solved crystal structures of both H-RAS^{A59E} and K-RAS^{A59E} in different nucleotide-bound states (Figure S2B and Table 2). Our crystals represented different stages of nucleotide exchange induced by Glu59. As demonstrated by H-RA-S^{A59E}, Glu59 repels switches I and II from the active site and weakens inter-switch β sheet interactions, regardless of the nucleotide (dashed circle in Figure 3B; Figure S3A). Moreover, Glu59 alters active site solvation, which in turn

influences Mg^{2+} and GDP stability (gray dashes in Figure 3C). First, repulsion of switch I by Glu59 breaks a canonical Tyr32-Tyr40 H-bond observed in wild-type H-RAS (magenta dashes at (1) in Figure 3C), allowing Glu59 to interact with Mg^{2+} and drawing switch II toward Lys16 and the P loop (orange dashes at (2) in Figure 3C). This creates a network that stabilizes active site opening and draws Lys16 and Mg2+ away from GDP (magenta dashes at (3) in Figure 3C).

The impact of Mg^{2+} release is demonstrated by K-RAS^{A59E}, which appeared to be an intermediate of intrinsic exchange and which was similar to the crystal structure of K-RAS^{A146T}, a mutant that also exhibits fast GEF-independent nucleotide exchange (Poulin et al., 2019). The active site of K-RAS^{A59E} is completely open and lacks Mg^{2+}, with switches I and β2 peeled away from the globular domain to form a novel β sheet (orange arrow in Figure 3D). Mg^{2+} dissociation allows β3 to extend toward switch II and Glu59 and Asp57 to make salt bridges with the P loop and K16, respectively (magenta dashes in Figure 3E). From the novel β sheet, β2 leads into the inter-switch loop 3 with rearrangement of salt bridges between Arg164, Asp47, and Glu49 at the junction of switch I and helix 1 (dashed circle in Figures 3D and S3B). Ultimately, these changes remove pi-stacking interactions between Phe28 in switch I and the guanine base of GDP, increasing solvent exposure of the nucleotide (Figures 3E and S3C). The details of our A59E crystal structures are consistent with the peak broadening of switch I and II resonances observed in our HSQC spectra of K-RAS^{A59E}, and this was particularly obvious after mapping the mutation-induced chemical shift perturbations onto the crystal structure of K-RAS^{A59E} (Figure 3F).

Our data suggest a mechanism of "Mg^{2+} extraction" that supports hyperexchange by autophosphorylated K-RAS^{A59T} and, possibly, other autophosphorylating GTPases. To explore this possibility, we used MD simulations to examine the dynamic relationship of position 59, Mg^{2+}, and GDP. Residue 59 C_β atom motions in K-RAS^{A59T} showed that both the mutation and the charge associated with phosphorylation shift residue 59 and switch II into the active site (Figures 3G, 3H and S3D). These results are consistent with simulations for other autophosphorylating GTPases (Figures 3I and S3E). Together, our data show that negative charge at position 59 destabilizes the Mg^{2+}-GDP interaction.

"Mg^{2+} extraction" appeared to represent an intermediate step in the process of adopting the conformation seen in our crystal structure of K-RAS^{A59E}, as the overall changes in K-RAS structure and dynamics seen in our NMR experiments were more consistent with the K-RAS^{A59E} crystal structure than the H-RAS^{A59E} crystal structures (Figure 3F). This explains why K-RAS^{A59Tp} and K-RAS^{A59E} have different kinetics of nucleotide exchange compared to K-RAS^{A59T}. While K-RAS^{A59T} locally influences switch I and II dynamics around the nucleotide to enhance exchange (upper versus lower, Figure 3F), the overall conformation is still recognizable to SOS1. In contrast, the extended and open active site conformation of K-RAS^{A59E}, and presumably K-RAS^{A59Tp}, is resistant to recognition and complex formation by SOS1.

Because of the extensive broadening of resonances, our NMR experiments do not provide direct evidence for the β sheet structure seen in the K-RAS^{A59E} crystal; however, the extended and open active site conformation stabilized by Glu59 shares the same global

conformation as crystal structures of K-RAS^{A146T} and wild-type K-RAS (Dharmaiah et al., 2019; Poulin et al., 2019). Taken together, these observations suggest that the extended and open conformation is likely present in wild-type K-RAS, but is less favored and in conformational equilibrium with other active site states. Furthermore, Glu59 directly stabilizes the extended and open conformation in K-RAS^{A59E} through an additional salt bridge (Figure 3E).

Finally, our structural analysis suggests two important points regarding the mechanism of RAS nucleotide exchange. First, the active site of RAS opens more than is necessary for intrinsic exchange of GDP for GTP, as K-RAS^{A59T}, K-RAS^{A59Tp}, and K-RAS^{A59E} all converge on similar rate constants for this reaction (Figure 1G). Second, the mechanism of SOS1-catalyzed nucleotide exchange is similar, but not identical, to the intrinsic mechanism of nucleotide exchange. Thus, our different biophysical and theoretical approaches argue that introduction of a Ser or Thr functional group at “residue 59” alters the enzymatic function of small GTPases to enable autophosphorylation, which permanently alters active site dynamics to favor intrinsic nucleotide exchange.

Autophosphorylation functionally activates K-RAS

The active site dynamics of K-RAS^{A59Tp} and K-RAS^{A59E} necessary for nucleotide exchange appear to be at odds with GTPase function, as small GTPases undergo closure of the active site to interact with their known effectors (Vetter, 2017). Nevertheless, the fact that Ala59 mutations occur in cancer suggest that they functionally activate K-RAS. To address this paradox, we first examined K-RAS^{A59T} function in SNU-175 cells expressing a doxycycline-inducible short hairpin RNA (shRNA) targeting the *KRAS* transcript. Knockdown of K-RAS in SNU-175 cells reduced proliferation and ERK phosphorylation, indicating that Thr59 does promote a proliferative function for K-RAS (Figures 4A, 4B, and S4A). At the same time, knockdown of K-RAS resulted in an increase in the fraction of K-RAS^{A59T} that was phosphorylated because phosphorylated KRAS^{A59T} accumulates over time as translation is inhibited (Figure 4C), as has been demonstrated for v-H-RAS (Ulsh and Shih, 1984). This result confirms the independent and passive nature of K-RAS^{A59T} autophosphorylation. To validate these observations in an independent system, we used CRISPR editing to insert the A59T mutation into the *Kras* locus of mouse embryonic stem (mES) cells (Figures S4B and S4C) and found that endogenous expression of K-RAS^{A59T} increases the phosphorylated state of MEK, ERK, and AKT (Figure 4D).

While our knockdown and knockin experiments demonstrated the ability of A59T mutation to activate K-RAS, we next tested the relative activity and transforming potential of Ala59 mutants, with and without co-mutation of G12V, by ectopic expression in NIH 3T3 fibroblasts (Figure S4D). Ectopic expression of each of the K-RAS mutants caused fibroblasts to exhibit a spindle-shaped morphology with elongated processes and refractile cytoplasm (Figure S4E), consistent with transformation. We also found that K-RAS^{A59E} showed a greater ability to transform fibroblasts than K-RAS^{A59T} (Figures 4E, S4F, and S4G), suggesting that negative charge, and not just Ala59 mutation, conferred transformation. Likewise, we noted that transformation by K-RAS$^{G12V/A59T}$ was enhanced compared to K-RAS^{A59T}. Nevertheless, both Ala59 mutations alone promoted

cell proliferation to a lesser extent than K-RAS^{G12V}, which was surprising given the strong effect that A59T and A59E have on GTP hydrolysis and nucleotide exchange (Figures 1F and 1G).

To understand these differences in fibroblast transformation, we examined activation of the MAPK and AKT signaling pathways. We first measured the ability of K-RAS to interact with the RAS binding domain of C-RAF (C-RAF-RBD), which recognizes and binds to GTP-bound RAS. C-RAF binding by K-RAS^{A59T} was more similar to wild-type K-RAS, and K-RAS^{A59Tp} failed to interact with C-RAF-RBD at all (Figure 4F). Likewise, co-mutation of A59T with G12V selectively enhanced the pull-down of the non-phosphorylated protein only (Figure 4G). Consistent with our pull-down experiments, activation of AKT and phosphorylation of its downstream target Rps6 was enhanced by co-mutation with G12V (Figures 4H and S4H–S4J). In contrast, K-RAS^{A59T} showed an intermediate activation of AKT and Rps6, while K-RAS^{A59E} expression induced no change at all (Figures 4H and S4I). However, we found that while all the K-RAS mutants induced similar levels of MEK phosphorylation in dividing fibroblasts, this activity poorly correlated with binding of C-RAF-RBD to Ala59 mutants (Figures 4I and S4I–S4L). Thus, K-RAS^{A59T} and K-RAS^{A59Tp} appear disparate in their ability to interact with C-RAF, alter cell signaling, and initiate fibroblast transformation.

Because K-RAS^{A59E} binds C-RAF-RBD, but K-RAS^{A59Tp} does not, we examined the dynamics of MAPK signaling in more detail. Strong activation of the MAPK signaling pathway can be detected by measuring hyperphosphorylation of C-RAF (Dougherty et al., 2005). Unlike fibroblasts expressing K-RAS^{A59T} and K-RAS^{G12V}, K-RAS^{A59E} does not induce C-RAF hyperphosphorylation (Figures 4J and S4I), and ERK phosphorylation was not significantly upregulated by K-RAS^{A59E} in dividing fibroblasts (Figures 4K and S4I). Thus, while our experiments broadly demonstrate cell transformation by K-RAS^{A59T} and K-RAS^{A59E}, their oncogenic activity is potentially limited by active site dynamics that alter their abilities to interact with specific effectors, essentially creating hypomorphic activating mutations.

Autophosphorylation influences K-RAS effector interactions

Our data indicated that residue 59 phosphorylation might inhibit effector binding because of its influence on switches I and II, which participate in effector binding (yellow surfaces in Figure 5A). To test this, we preloaded mutant K-RAS protein from our NIH 3T3 lysates with nucleotide and again tested them for interaction with C-RAF-RBD or, additionally, with full-length RASSF5 protein. These effector interactions provide complementary information because C-RAF-RBD interacts exclusively with switch I, while RASSF5 interacts with both switches I and II. We found that Thr59 phosphorylation inhibits binding to C-RAF and RASSF5, while A59E selectively inhibits binding to RASSF5 (Figure 5B). Notably, under these experimental conditions K-RAS^{A59T} was able to bind C-RAF and RASSF5 (red versus black arrows in Figure 5B).

Because our GppNHp-bound H-RAS^{A59E} crystal structures have disordered active sites, we used MD simulations to explain why K-RAS^{A59Tp} and K-RAS^{A59E} appeared to behave differently. We noted that simulations of GDP-bound K-RAS^{A59Tp} exhibited low frequency

conformations with the phosphoryl group facing away from the active site (arrow in Figures 3G and 3H). Likewise, while GTP-bound wild-type K-RAS and K-RAS^{A59T} had similar overall dynamic profiles (Figures S5A and S5B), the phosphoryl group of K-RAS^{A59Tp} bound to GTP showed a clear transition out of the active site, repulsing Glu37 (arrows in Figures 5C and 5D). In contrast, GTP-bound K-RAS^{A59E} did not make this transition (Figures 5C and S5C), and instead switch interactions are enhanced, as Glu37 in switch I and Arg68 in switch II interactduring the simulation. Except for ARL6 and DIRAS1, phosphoryl transitions in the other GTPases and their overall effects on switches I and II were like phosphorylated K-RAS^{A59T} (Figure S5D).

Thus, the GTP-bound states of K-RAS^{A59T} and K-RAS^{A59E} were likely underestimated in our initial RAS activity assays because autophosphorylation impacts the affinity of RAS-RAF interaction (Figure 4F). To address this directly, we tested RAF binding activity of K-RAS^{A59T} and K-RAS^{A59E} using bioluminescence energy transfer (BRET) in cells with the regulatory domains of the RAF isoforms (Terrell et al., 2019). The regulatory domain of each RAF isoform consists of a variable N-terminal segment followed by the RBD and a cysteine-rich domain (CRD), which together bind RAS (Cookis and Mattos, 2021; Tran et al., 2021). Like our binding experiments with C-RAF-RBD, K-RAS^{A59T} and K-RAS^{A59E} exhibited reduced affinity for the regulatory domains of C-RAF, A-RAF, and B-RAF relative to K-RAS^{G12V} and K-RAS^{G12D} (Figures 5E, 5F, S6A and Table S2). The status of MEK phosphorylation in serum-starved cells expressing K-RAS^{A59T} or K-RAS^{A59E} trended with C-RAF co-immunoprecipitation (Figure 5F), reflecting the graded differences in fibroblast proliferation induced by K-RAS^{A59T} and K-RAS^{A59E} and altered kinetics of MAPK signaling seen in our dividing NIH 3T3 cells (Figures 4E, 4J, 4K, and S4L).

Recent crystal structures of RAS in complex with C-RAF-RBD-CRD (Cookis and Mattos, 2021; Tran et al., 2021), as well as NMR-data-driven models of K-RAS and the RBD-CRD tethered to nanodiscs (Fang et al., 2020), suggest Ala59 mutations would predominantly affect interactions with the RBD domains of the three RAF isoforms (Figures S6B and S6C). Using biolayer interferometry (BLI), we found that each RAF-RBD has a reduced affinity for K-RAS^{A59T} and K-RAS^{A59E} (Figures 5G and S6D).However, the affinities of Ala59 mutants for A-RAF and C-RAF measured by BRET (i.e., $BRET_{50}$) were not consistent with our BLI and co-immunoprecipitation data. While differences in B-RAF colocalization with K-RAS^{A59T} and K-RAS^{A59E} also reflect differences in their GTP-bound state (Figure 4F), colocalization with C-RAF, and more so A-RAF, appears less dependent on K-RAS^{A59T} or K-RAS^{A59E} interacting with their respective RBDs. Because BRET can be induced by distances of <100Å (Boute et al., 2002), it is possible that the association of K-RAS with C-RAF or A-RAF may be facilitated by other factors.

While B-RAF exhibits weak association with K-RAS^{A59T} and K-RAS^{A59E}, it could still be activated through heterodimerization with C-RAF (Freeman et al., 2013). We tested this possibility and found that K-RAS^{A59T} and K-RAS^{A59E} showed a barely detectable increase in C-RAF/B-RAF heterodimerization compared to wildtype K-RAS (Figure 5H). Our data suggest that K-RAS^{A59T} and K-RAS^{A59E} likely do not activate MAPK signaling through B-RAF/C-RAF heterodimerization, but rather through weak activation of A-RAF

and C-RAF. Further, these data are consistent with the altered kinetics of MAPK signaling seen in our dividing fibroblasts (Figures 4E, 4J, 4K, and S4L).

The reduction in RASSF5 binding in response to Ala59 mutation was also noteworthy. RASSF5 is a member of a putative tumor suppressor family associated with growth inhibition downstream of activated RAS (Volodko et al., 2014). In agreement with a recent report (Dhanaraman et al., 2020), we discovered that only RASSF1 and RASSF5 exhibit affinity for active K-RAS and that K-RAS^{A59Tp} and K-RAS^{A59E} appeared to specifically affect the interaction with RASSF5 (Figures S7A and S7B). The functional activation of K-RAS—i.e., its induction of proliferation—by Ala59 mutations might be due to its weak activation of pro-proliferation signaling and its lack of activation of anti-proliferation signaling.

For small GTPases, increased active site dynamics in the GTP-bound state, along with phosphorylation that changes active site compaction and organization, will necessarily alter effector affinity and kinetics of complex formation. This is demonstrated by comparison of our MD simulations to crystal structures of RAS bound to C-RAF-RBD (Figure 5I) and RASSF5 (Figure S7C). For instance, in solution, K-RAS^{A59T} shows weak affinity for the RAF isoforms and RASSF5 (Figures 5G and S7A). For RAF, this makes sense because our MD simulations of K-RAS^{A59T} show that Thr59 association with GTP is disruptive to Thr35 packing in the active site (Figures 2C and S2F), and it is well known that Thr35 mutants of RAS have reduced affinity for C-RAF due to enhanced switch I dynamics (Spoerner et al., 2001). After Thr59 phosphorylation, dynamics in switches I and II increase, preventing RAF (and presumably RASSF5) binding to K-RAS^{A59Tp} (Figures 5I and S7C). Changes in RAF affinity appear to be specific for K-RAS^{A59T} and K-RAS^{A59E} because H-RAS^{A59G} and K-RAS^{A59G}, which have similar changes in GTP hydrolysis and nucleotide exchange, maintain high affinity for RAF (Hall et al., 2001; Lu et al., 2018). It remains unclear why the Ala59 mutants studied here disrupt binding to B-RAF more so than A-RAF or C-RAF (Figure 5G).

A notable difference between K-RAS^{A59E} and K-RAS^{A59Tp} was that K-RAS^{A59E} was capable of binding C-RAF (Figure 5B). This is likely due to the Glu59 inducing less dynamical changes in switch I and changes in switch II being less important for RAF interaction (Figures 5I, S6B, and S6C). Differences in the movement of Glu37 in our MD simulations of K-RAS^{A59E} and K-RAS^{A59Tp} are also consequential because Glu37 mutants inhibit binding to C-RAF (Hamad et al., 2002).

Nevertheless, changes in switch dynamics also contribute to impaired binding of K-RAS^{A59E} and K-RAS^{A59Tp} to RASSF5. For the K-RAS^{A59T}/RASSF5 interaction, weakened affinity can be explained by the expanded binding interface of RASSF5, which is very sensitive to changes in active site compaction (Stieglitz et al., 2008). The addition of negative charge at the RASSF5 binding interface also plays an important role. For instance, the E37G mutation, which reduces the affinity of RAS proteins for RalGDS, improves binding of RAS to RASSF5 (Hamad et al., 2002; Khokhlatchev et al., 2002). Thus, repulsion of Glu37 by Glu59, or phosphorylated Thr59, further inhibits binding of RASSF5 to K-RAS^{A59E} and K-RAS^{A59Tp} (Figures 5B, S7A, and S7B). This rationale can be extended

to interactions with PI3K and Sin1, part of the mTORC2 complex, because, like RASSF5, they form extended interactions with switch II (Figures S6E and S6F). Thus, differences in AKT phosphorylation in our fibroblast transformation experiments (Figure 4I) could be due to a failure of Ala59 mutants to recruit and associate with PI3K and mTORC2 (Castel et al., 2021; Castellano and Downward, 2011; Kovalski et al., 2019). Together, these data demonstrate that a consequence of GTPase autophosphorylation is to alter effector engagement.

DISCUSSION

Here, we elucidate the mechanistic basis for the autophosphorylation of small GTPases and determine the effect of this modification on the GTPase cycle. The functional state of a GTPase is presumed to be a function of its nucleotide binding state (Figure 6A). In the canonical GTPase cycle, intrinsic and GEF-induced nucleotide exchange activate the protein by loading GTP into the active site, while intrinsic and GAP-induced GTP hydrolysis serve to inactivate. Using K-RAS^{A59T} as an architype for small GTPases that are capable of autophosphorylation, we show that phosphorylation at position 59 alters active site dynamics, nucleotide exchange, and effector interaction to dramatically reorganize the GTPase cycle (Figure 6B). Although the ability of H-RAS^{A59T} to autophosphorylate has been known for some time, our study disproves one of the initial presumptions of this biochemical activity—that it is simply a byproduct of the hydrolysis reaction.

An intriguing outcome of our study is that autophosphorylation enhances intrinsic exchange but desensitizes K-RAS to SOS1-catalyzed nucleotide exchange (Figure 1G), and this may explain why K-RAS^{A59T} shows weak cellular activation that is overcome by co-mutation of G12V (Figures 4F–4H). Moreover, phosphorylation of Thr59 creates a preference for GTP exchange over GDP exchange (Figure 1G). After GTP binding, K-RAS^{A59Tp} and K-RAS^{A59E} do undergo necessary dynamics to take on an active GTP-bound state, but with altered effector binding (Figure 6C). Altered interaction with RAF proteins likely limits pro-proliferation signaling downstream of K-RAS^{A59T} and K-RAS^{A59E}.

It is also possible that autophosphorylation allows for novel effector interactions, perhaps overlapping with the other small GTPases that potentially autophosphorylate. Indeed, DIRAS subfamily members can compete with K-RAS to bind to effector proteins (Bergom et al., 2016). Likewise, K-RAS^{A59T} may become susceptible to new regulation, as DIRAS1/2 are regulated by RapGAPs (Gasper et al., 2010). Thus, the unexpectedly low activation of K-RAS^{A59T}, compared to K-RAS^{A59E}, could be due to stimulation of GTP hydrolysis by alternate GAPs, whose activity is suppressed by co-mutation of Gly12. In support of this, a recent report shows that RGS3, a GAP of G-protein-coupled receptors, can catalyze hydrolysis of GTP bound to K-RAS^{G12C} (Li et al., 2021).

Our observations explain why Ala59 mutations are so rare in cancer despite their inhibition of GTP hydrolysis and increase of nucleotide exchange. Functional activation of K-RAS^{A59T} and K-RAS^{A59E} is likely limited by the mechanism of hyperexchange and its altered effector interactions, ultimately creating weakly activated mutants. Indeed, the attenuating function of Thr59 might be necessary for v-K-RAS and v-H-RAS to avoid

oncogene-induced senescence due to hyperactivated MAPK signaling or through binding to RASSF5 (Donninger et al., 2016). Consistently, we found that co-mutation of Ala59 and Gly12 enhanced Akt phosphorylation and activation of non-phosphorylated K-RAS in mouse fibroblasts, suggesting that autophosphorylation has a specific function. How K-RAS^{A59T} and K-RAS^{A59E} change the kinetics of activation and feedback regulation of the MAPK signaling pathway and their reliance on evasion of RASSF5 to promote cell transformation and tumorigenesis are questions that remain to be answered.

Because the field has yet to identify GEFs for many of the GTPases listed in Table 1, it is possible that autophosphorylation of threonine or serine at position 59 might replace these regulatory proteins (Foster et al., 1996). For GTPases capable of autophosphorylation, altered nucleotide binding cycle is likely an aspect of their normal regulation, creating a pool that is functionally distinct from the non-phosphorylated pool. We also noted that some of these small GTPases have cancer-associated mutations at their analogous residue 59 (Table 1), which would render them unable to autophosphorylate and perhaps alter their GTPase cycles back toward the more canonical form.

The most thoroughly characterized RAS modifications (e.g., phosphorylation, di-ubiquitination) regulate its subcellular localization, typically pushing it from the plasma membrane to organellar endomembranes (Ahearn et al., 2018). But others (e.g., monoubiquitination, acetylation, AMPylation, tyrosyl phosphorylation) are reported to affect the GTPase cycle by influencing nucleotide exchange (Barthelmes et al., 2020; Kano et al., 2019; Sasaki et al., 2011; Ting et al., 2015; Yang et al., 2012). Indeed, our work has parallels with a recent proposal that Src shifts K-RAS into a “dark state” through phosphorylation of Tyr32 and Tyr64. *In vitro* characterization demonstrated that Tyr phosphorylation enhances the GTP-bound population of K-RAS but simultaneously impairs binding to RAF kinases (Kano et al., 2019). However, our study differs from that of Kano et al. in that phosphorylation of residue 59 still promotes functional activation of K-RAS. Thus, our work illuminates a new paradigm for regulation of the GTPase cycle via autophosphorylation. This discovery opens the door to a deeper look at the PTM landscape on GTPases and more detailed studies of their functional ramifications.

Limitations of the study

Our studies used K-RAS^{A59E} to mimic K-RAS^{A59Tp}. While neither glutamate nor aspartate can fully recapitulate the charge and shape of phospho-threonine, we did find that K-RAS^{A59Tp} and K-RAS^{A59E} shared a couple of key traits. First, both prefer intrinsic over SOS1-mediated nucleotide exchange. Second, both affect switch II conformation and dynamics such that RASSF5, and likely PI3K and Sin1, are incompatible binding partners. Unlike K-RAS^{A59E}, however, K-RAS^{A59Tp} prefers GTP over GDP and cannot bind RAF. Thus, more work will need to be done to elucidate the subtle differences between Ala59 mutations.

While several GTPases share the ability to autophosphorylate when mutated to serine or threonine at the correct active site position, experimental validation of autophosphorylation by the GTPases in Table 1 was not included in this work. However, this study shows that most of these GTPases should be capable of this reaction, as their respective residue 59

nucleophiles move toward the γ-phosphate. Further studies of the GTPases in Table 1 need to be performed.

STAR★METHODS

RESOURCE AVAILABILITY

Lead contact—Further information and requests for data and resources should be directed to the lead contact, Dr. Kevin Haigis (mailto:Kevin_haigis@DFCI.harvard.edu).

Materials availability—Plasmids generated by this study are available upon request.

Data and code availability

- Original scans of western blot data have been deposited at Mendeley Data and are publicly available as of the date of publication. Validation reports of X-ray crystallography structures have been deposited at the PDB and are publicly available as of the date of publication. DOIs are listed in the key resources table.
- This paper does not report original code.
- Any additional information required to reanalyze the data reported in this paper is available from the lead contact upon request.

EXPERIMENTAL MODEL AND SUBJECT DETAILS

Cell lines—All cell lines were cultured at 37°C, ~95% humidity, and 5% CO_2. Short tandem repeat (STR) genotyping, performed by LabCorp, was done to ensure cell line authenticity.

SNU-175 and LIM1215 cells—Cells were cultured in RPMI containing 10% FBS and 1% PenStrep. Cells were maintained according to published protocols (Ku and Park, 2005; Oh et al., 1999; Whitehead et al., 1985).

HEK293t, HEK293FT, and NIH 3T3 cells—Cells with cultured in DMEM containing 10% FBS and 1% PenStrep. Cells were split every 2–3 days.

HeLa cells—Cells with cultured in EMEM containing 10% FBS and 1% PenStrep. Cells were split every 2–3 days.

Mouse embryonic stem (mES) cells—K-Ras$^{+/LSL\text{-}wildtype}$ and K-Ras$^{A59T/LSL\text{-}A59T}$ mES cells were cultured on both commercial and homemade irradiated feeder MEFs (1.5–2.0×10^6 cells per gelatin coated 10cm dish). Cells were grown in the following media: 425 mL of GIBCO Knockout DMEM, 75 mL of heat inactivated HyClone Fetal Bovine Serum, 5 mL 100x Glutamax, 3.5 μL of 14.3 M Mercaptoethanol, 5 mL 100X MEM non-essential amino acid solution, 5 mL 100X PenStrep, and 1 μL/mL of ESGRO Leukemia inhibitory factor (LIF). mES colonies were grown until visible to the naked eye before splitting. Cell media was refreshed every day, and always 2–3 h before sub-culture, clone picking, or nucleofection.

METHOD DETAILS

Sequence alignment of small GTPases with autophosphorylation motif— *S*equences for K-RAS, ARL6, DIRAS1, DIRAS2, RAB40A, RAB40B, RAB40C, RASD1, RASD2, RND1, RND2, and RND3 were extracted from the NCBI database (Coordinators, 2016). Alignments were done using the T-COFFEE algorithm provided by SnapGene® software (GSL Biotech).

Bottom-up mass spectrometry—Approximately 20 μg of purified 6xHis-tagged K-RAS4B^{A59T} were reduced with 5 mM tris(2-carboxyethyl)phosphine for 30 min at room temperature, alkylated with 10 mM iodoacetamide for 30 min at room temperature in the dark, and quenched with 10 mM dithiothreitol for 15 min at room temperature. The sample was divided into two replicates, precipitated by trichloroacetic acid precipitation, and digested with 1:50 (w/w) chymotrypsin in 100 mM Tris-HCl and 10 mM $CaCl_2$ for 18 h at 37°C with shaking. The samples were desalted using a StageTip, dried by vacuum centrifugation and solubilized in 5% acetonitrile and 5% formic acid. LC-MS/MS analysis was performed on a Q Exactive mass spectrometer coupled with a Famos Autosampler and an Accela600 liquid chromatography pump. Peptides were separated on a 100 μm inner diameter microcapillary column packed with :25 cm of Accucore C18 resin (2.6 μm, 150 Å). For each analysis we loaded ~1 μg onto the column.

Peptides were separated using a one-h method of 5%–25% acetonitrile in 0.125% formic acid with a flow rate of :300 nL/min. The scan sequence began with an Orbitrap MS^1 spectrum with the following parameters: resolution 70,000, scan range 300–1500 Th, automatic gain control target 1×10^5, maximum injection time 250 ms, and centroid spectrum data type. We selected the top twenty precursors for MS^2 analysis which consisted of high-energy collision dissociation with the following parameters: resolution 17,500, AGC 1×10^5, maximum injection time 60 ms, isolation window 2 Th, normalized collision energy 30, and centroid spectrum data type. The underfill ratio was set at 1%, which corresponds to a 1.1×10^4 intensity threshold. Unassigned and singly charged species were excluded from MS^2 analysis and dynamic exclusion was set to automatic.

Spectra were searched using Sequest with a 3 ppm precursor mass tolerance, 0.03 fragment ion tolerance, and no limit on internal cleavage sites (Eng et al., 1994). Cysteine alkylation was set as a fixed modification, methionine oxidation and phosphorylation of serine, threonine, and tyrosine were included as variable modifications. Spectra were searched against a custom database containing the K-RAS4B^{A59T} sequence, common contaminants, and the reversed peptide sequences. False discovery rate was estimated by linear discriminant analysis and applied at one percent at the peptide level (Elias and Gygi, 2007; Peng et al., 2003).

Molecular dynamics simulations—Starting coordinates for molecular dynamic simulation were generated from the crystal structures published here and from the PDB. For simulations of GDP-bound or GTP-bound K-RAS, we used the starting wild-type structures 6MBU (Dharmaiah et al., 2019) and 4DSO (Maurer et al., 2012). Starting PDB coordinates for RND1, RND3, DIRAS1, DIRAS2, and ARL6 were 2CLS, 1M7B (Fiegen

et al., 2002), 2GF0, 2ERX, and 2H57, respectively. Starting structures went through an extra round of modeling and refinement to add in missing residues and remove alternate conformations. Structures were converted into the GDP- or GTP-bound states, or mutated, *in silico*. Preparation of starting files, including 'residue 59' phosphorylation was done using 'solution builder' available from CHARM-GUI (Brooks et al., 2009; Jo et al., 2008; Lee et al., 2016). Charged residues, including protein termini, were protonated or deprotonated in accordance with neutral pH. A cubic box with edges 10 Å from each protein was created and filled with TIP3P water molecules and neutralized with Cl^- and Na^+ ions to 150 mM. Minimizations, equilibrations, and simulations were done using GROMACS (ver. 2020.1) and a GPU server featuring 8x Tesla v100 workstation, on the O2 High Performance Compute Cluster, supported by the Research Computing Group, at Harvard Medical School. Solvated systems were energy minimized by steep integration for 5000 steps or at a maximum force of 1000 kJ/mol/nm or less. The Verlet cutoff scheme was used for nonbonded atoms and the LINCS algorithm was applied to covalent H-bonds. Short-range van der Waals interactions were switched off from 1.0–1.2 nm, and long-range interactions were computed using the Particle Mesh Ewald method. Simulation temperatures were maintained at 310K using Nose-Hoover extended ensemble. The isothermal-isobaric ensemble (NPT) was generated using the Parrinello-Rahman barostat method with periodic boundary conditions. Simulations were done for 800–900 ns using the GROMOS force-field.

Validation and analyses steps were done in GROMACS, including cluster analysis using the GROMOS algorithm (Daura et al., 1999). Distance measurements and visual analyses were done using PyMOL and VMD (Humphrey et al., 1996). Frequency distributions that depict the distances between atoms throughout the simulations were calculated using a 0.20Å bin cutoff in PRISM.

Protein purification for biochemical assays—Human K-RAS4B and the catalytic domains of GAP (715–1047) and SOS11 (564–1049) were synthesized with N-terminal hexa-histidine tags (6xHis) and inserted in the pET21a plasmid for *E. coli* expression by GENEWIZ. K-RAS mutants (i.e., G12D, A59T, A59E, A59S, A59H, and A59Y) were made by site-directed mutagenesis. All expressed K-RAS proteins were full-length with the C-terminal two amino acids removed to mimic post-translational processing (Hancock et al., 1991). Protein expression was done using chemically transformed BL21 (DE3) strain of *E. coli* and Terrific Broth media. A 30mL culture of broth was inoculated with BL21 *E. coli* cells with the appropriate tagged protein and allowed to grow overnight at 37°C with agitation. The following morning 25mL of culture was applied to a 1L culture of terrific broth, and protein expression was induced with 120mg/L of IPTG after *E. coli* reached an O.D. 0.8. After 6 h at 37°C the cell solution was centrifuged at 10,000RPM at 4°C and pellets were stored at −80°C. His-tagged protein was purified from *E. coli* paste as follows. Frozen pellets were re-suspended in sterile filtered buffer TA (20 mM Tris pH 7.5, 50 mM NaCl, 5 mM $MgCl_2$, 5% glycerol, 10 μM GDP, 156 mL/L 2-mercaptoethanol) containing 4 mM PMSF at < 0.5mg/mL by agitation at room temperature for 15–30 min. *E. coli* cells were lysed by sonication on ice. Lysate was then clarified for 30 min at 4°C and 14,000 RPM. Chromatography of supernatant was done using an AKTA FPLC. Supernatant was

first subjected to immobilized metal affinity chromatography (IMAC) using a 5 mL Hi-Trap TALON column. The running buffer for IMAC was buffer TA, and sterile buffer TB (20 mM Tris pH 7.5, 50 mM NaCl, 5 mM $MgCl_2$, 200 mM Imidazole, 5% glycerol, 10 μM GDP, 156 μL/L of 2-mercaptoethanol) was used for gradient elution. Post-elution, positive fractions were screened by SDS-PAGE, pooled and concentrated to < 1mL using a 10,000 kDa Amicon Ultra spin concentrator. Concentrated protein was then buffer exchanged into QA buffer (20 mM Tris pH 8.0, 50 mM NaCl, 5 mM $MgCl_2$, 5% glycerol, 10 μM GDP, 156 μL/L 2-mercaptoethanol) using a ZEBA spin column per manufacturer protocol. Buffer exchanged protein was applied to a 5 mL HiTrap QHP column using a 30% gradient of QB buffer (20 mM Tris pH 8.0, 1.0 M NaCl, 5 mM $MgCl_2$, 5% glycerol, 10 μM GDP, 156 μL/L 2-mercaptoethanol) over 60 mL. Positive fractions were then pooled and subjected to buffer exchange twice using ZEBA spin columns. The first exchange was into protein into stabilization buffer (20 mM Tris pH 7.5, 10 mM NaCl, 1 mM $MgCl_2$, 1% glycerol, 1 mM DTT) containing 5 mM EDTA and then protein was re-exchanged into stabilization buffer without EDTA. Protein concentration was then determined, and equimolar GDP was added to KRAS4B protein. Protein for nucleotide hydrolysis and exchange were diluted to approximately 100μM, including GAP334 and SOS1cat, flash frozen in liquid nitrogen in 50–150 μL aliquots for single use, and then stored at −80°C. To obtain phosphorylated K-RAS4B, after the IMAC step, K-RAS4B^{A59T} was incubated overnight or longer in the presence of GTP, and then purification was continued. Post-QHP, phosphorylated protein was identified by SDS-PAGE and pooled separately from the non-phosphorylated form.

Crystallization of Ala59 mutants of H-RAS and K-RAS—Purification and crystallization of truncated (residues 1–166) and untagged H-RAS^{A59T} and H-RAS^{A59E} was done using a previously published protocol (Johnson et al., 2015). H-RAS^{A59T} bound to GppNHp was concentrated to 12.1 mg/mL, flash frozen, and stored at −80°C before crystallization. H-RAS^{A59E} bound to GppNHp and GDP were stored the same way but concentrated to 18.1 and 15.2 mg/mL, respectively. All crystals were grown using reagents from Hampton Research. Crystals were grown using the hanging drop vapor diffusion method in 24-well plates sealed with Vaseline at 18°C. Mother liquor constitution was unique for each crystal grown, and each crystal was grown against a mother liquor well volume of 402 μL. Crystals were harvested at 2–4 weeks and flash frozen using mother liquor with 30% glycerol. The first crystal of H-RAS^{A59T} bound to GppNHp was crystallized in 2 μL by2 μL drops using the following reservoir solution: 2.6 mM NaCl, 1.0 mM $MgCl_2$, 15.7 mM HEPES pH 7.5, 2.5 mM DTT, 37.3 mM $Ca(OAc)_2$ and 20.5% PEG 3350. The second crystal of H-RAS^{A59T} was crystallized in 1 μL by 1 μL drops using the following reservoir solution: 10 mM $Mg(OAc)_2$, 44.8% PEG400, 15.7 mM HEPES pH 7.5, 1.0 mM $MgCl_2$, 3.4 mM NaCl, and 2.5 mM DTT. H-RAS^{A59T} crystals contained one molecule of H-RAS^{A59T} in the asymmetric unit and exhibited $P3_221$ symmetry. H-RAS^{A59E} bound to GDP was crystallized in 1 μL by 1 μL drops using the following reservoir solution: 2.6 mM NaCl, 1.0 mM $MgCl_2$, 15.7 mM HEPES pH 7.5, 2.5 mM DTT, 43.5 mM $Ca(OAc)_2$, and 20.5% PEG 3350. H-RAS^{A59E} bound to GppNHp was crystallized in 1 μL by 1 μL drops using the following reservoir solution: 2.6 mM NaCl, 1.0 mM $MgCl_2$, 15.7 mM HEPES pH7.5, 2.5 mM DTT, 9.95 mM $Ca(OAc)_2$, and 19.9% PEG 3350. Both H-RAS^{A59E} crystals contained two molecules in the asymmetric unit, but GppNHp crystals

grew with $P12_11$ symmetry while the GDP crystals grew with P1 symmetry. Data collection for all crystals was done on a home source MicroMax007HF with Cu^{2+} anode and tungsten filament, and a R-Axis IV^{2+} detector from Rigaku. Indexing, integration and scaling data processing steps were done using the HKL3000 package (Otwinowski and Minor, 1997). For molecular replacement, a previously refined model of wild-type H-RAS (PDB code 1CTQ) was used for both H-RAS^{A59T} and H-RAS^{A59E} crystals bound to GppNHp (Klink and Scheidig, 2010). H-RAS^{A59E} bound to GppNHp was used as starting models for the H-RAS^{A59E} GDP structures. A single round of simulated annealing was performed before refinement. Molecular replacement and structure refinement was done use the PHENIX program (version 1.11.1–2575) (Adams et al., 2010).

Protein for crystallization of K-RAS^{A59E} bound to GDP was acquired by a different purification scheme than above. His-tagged K-RAS4B^{A59E} was overexpressed in *E. coli* BL21 (DE3) and purified in the presence of 20 μM GDP. Briefly, cells were grown at 37°C in TB medium in the presence of 100 μg/mL of ampicillin to an OD of 0.8, cooled to 17°C, induced with 500 μM IPTG, incubated overnight at 17°C, collected by centrifugation, and stored at −80°C. Cell pellets were lysed in buffer A (25 mM HEPES, pH 7.5, 500 mM NaCl, 5 mM MgCl2, 5% glycerol, 20 mM GDP, 7 mM 2-mercaptoethanol, and 20 mM Imidazole), and the resulting lysate was centrifuged at 30,000 g for 40 min. Ni-NTA beads (QIAGEN) were mixed with cleared lysate for 30 min and washed with buffer A. Beads were transferred to an FPLC-compatible column, and the bound protein was washed further with buffer A for 10 column volumes and eluted with buffer B (25 mM HEPES, pH 7.5, 500 mM NaCl, 5 mM MgCl2, 5% glycerol, 20 μM GDP, 7 mM 2-mercaptoethanol, and 400 mM Imidazole). The eluted sample was concentrated, then 10-fold diluted in buffer C (20 mM Tris, pH 8.0, 200 mM NaCl, 5 mM MgCl2, 5% glycerol, 20 μM GDP, and 1 mM DTT), applied to Mono-Q column, and eluted by using 50–500 mM NaCl gradient. K-RAS containing fractions were concentrated and passed through a Superdex 75 16/600 column in a buffer containing 25 mM HEPES, pH 8.0, 200 mM NaCl, 5 mM MgCl2, 5% glycerol, 20 μM GDP, and 1 mM DTT. HRV 3C protease was added to KRAS mutants containing fractions and incubated overnight at 4°C, followed by passing through Ni-NTA column to remove His-tag and 3C protease. Fractions were pooled, concentrated to approximately 20 μg/mL (for LC-ESI-MS) or 40 mg/mL (for crystallization), and frozen at −80°C. For crystallization, a Formulatrix NT8, RockImager and ArtRobbins Phoenix liquid handler was used to dispense a 100 nL sample of 800 μM K-RAS^{A59E} with an equal volume of 1.5 M NaMalonate and 0.1 M HEPES pH 7.5 for crystallization by sitting-drop vapor diffusion. Crystals were grown at 27°C for three days before harvest. Diffraction data were collected at beamline 24ID-E of the NE-CAT at the Advanced Photon Source (Argonne National Laboratory). Datasets were integrated and scaled using XDS (Kabsch, 2010). Structures were solved by molecular replacement using the program Phaser and the search model PDB entry 5TAR (Dharmaiah et al., 2016; McCoy et al., 2007). Iterative manual model building and refinement using Phenix and Coot led to a model with excellent statistics (Adams et al., 2010; Emsley and Cowtan, 2004). Statistics for all crystal data can be found in Table 1.

NMR spectroscopy—Isotopically ^{15}N labeled K-RAS (residues 1–185 of K-RAS4B with a C118S substitution bearing A59T or A59E substitutions or wild-type A59) was expressed

with an N-terminal His-tag from the pET28 vector in the *E. coli* strain BL21 (DE3 Codon$^+$). A codon-optimized sequence encoding K-RAS4B was synthesized (GenScript) and the A59 codon was mutated using QuikChange site-directed mutagenesis (Agilent). Transformed bacteria was cultured at 37°C in M9 minimal media in the presence of kanamycin and chloramphenicol and supplemented with 1 g/L ^{15}N ammonium chloride until the $O.D._{600\ nm}$ reached 0.6. Protein expression was then induced with 0.2 mM IPTG (Isopropyl β-D-1-thiogalactopyranoside) at 155C overnight.

After centrifugation of the culture, the cell pellets were re-suspended with lysis buffer (50 mM Tris, 150 mM NaCl, 0.1% NP-40, 10% Glycerol, 10 mM Imidazole, 5 mM $MgCl_2$, 1 mM PMSF, 10mM β-mercaptoethanol and lysozyme at pH 8.0) and lysed by sonication. Following centrifugation, His-tagged K-RAS proteins were purified by Ni^{2+}-NTA column affinity chromatography from the soluble fraction, the buffer was exchanged to reduce the imidazole concentration, then K-RAS was further purified by size exclusion chromatography (Superdex™ S75 26–60 column) in a running buffer comprising 20 mM HEPES, 100 mM NaCl, 5 mM $MgCl_2$, and 2 mM tris(2-carboxyethyl)phosphine (TCEP), pH 7.4. RAS proteins naturally co-purify bound to GDP (Feuerstein et al., 1987), but the purity of K-RAS^{A59T} (i.e., lack of K-RAS^{A59Tp}) was confirmed by the NMR spectra (data not shown).

^{1}H-^{15}N HSQC spectra were collected with 8 scans at 25°C on a Bruker NEO III HD 800MHz spectrometer equipped with a 5 mm TXO CryoProbe. K-RAS samples were concentrated (wild-type: 500 μM; K-RAS^{A59T}: 360 μM; K-RAS^{A59E}: 500 μM) in size exclusion buffer plus 5% (vol/vol) D_2O. NMR data were processed and analyzed using NMRPipe (Delaglio et al., 1995) and CcpNmr (Vranken et al., 2005).

Chemical shift perturbations (CSPs, chemical shift changes of the NH cross-peaks of the A59T/E mutants relative to wild-type), were calculated using the formula $\Delta\delta NH.N(ppm) = Ö([(\Delta H)]^2+[(\Delta N/5)]^2)$ and plotted against residue number using GraphPad 9.1.0. The NH resonances of the mutants were assigned based on previous assignment of wild-type K-RAS (BMRB entry 27720) together with a 3D ^{15}N-edited NOESY HSQC spectrum (mixing time 120ms). Chemical shift changes were mapped onto the structure of wild-type K-RAS bound to GDP (PDB 6MBU) as well as our new structure of K-RAS^{A59E} using Chimera 1.15.

Autophosphorylation and dephosphorylation experiments—Phosphorylated β-casein was used as a positive control for Lambda Phosphatase (LMP) activity for dephosphorylation experiments. A solution of 90 μL of tagged K-RAS^{A59T} (or β-casein) at 10 mg/mL and 10 μL of GTP or GDP at 50 mg/mL were incubated overnight at 37°C. After overnight incubation, 10μL of the GTP and K-RAS^{A59T} mixture (or β-casein) was incubated at 30°C or 95°C for 10 min, and subsequent dephosphorylation was tested by adding 1.0 μL of this solution to 49 μL of 1x phosphatase buffer supplemented with $MnCl_2$ and either 400 units of LMP or water. Dephosphorylation was allowed to proceed for 2, 4, and 6 h at 30°C.

The kinetics of autophosphorylation were also done using purified K-RAS^{A59T} with SOS1 or GAP334. Autophosphorylation reactions were done using a 20X reaction buffer (1.0 M Tris-HCL, 20 mM $MgCl_2$, pH 7.5). Purified proteins were diluted to initial starting

concentrations of 250 μM K-RAS^{A59T} and 100 μM GAP and SOS1. For the K-RAS^{A59T} reaction without regulators, reactions were run at the following conditions: 2.5 μL of 20X reaction buffer, 5 μL GTP (25 mg/mL) dissolved in water, 1–16 μL of 250μM KRAS4B^{A59T} and finally balanced to 50 μL with Ultrapure water. For autophosphorylation in the presence of GAP and SOS1, the above reaction mixture was used, except 4 μL of 250 μM K-RAS^{A59T} was fixed for each reaction and 0.5–20 μL of purified regulator was added to each reaction and balanced with water to 50 μL. Each autophosphorylation experiment was done over 8 h at 37°C. Each h, a 2 μL sample was taken from each reaction and then added to 2 μL of 6X SDS-PAGE sample buffer and 8 μL of water. Samples were then boiled for 5 min at 70°C. Changes in phosphorylation were detected by 12.5% SDS-PAGE. While the dephosphorylation experiments were done using Coomassie blue staining, the kinetics of autophosphorylation were measured using western blot. Quantification was performed by measuring changes in the upper band versus the sum of the upper and lower bands.

To detect and compare autophosphorylation in K-RAS^{A59S}, K-RAS^{A59H}, and K-RAS^{A59Y} compared to wildtype K-RAS and K-RAS^{A59T}, proteins were purified using the Ni-NTA bead method (above). Purified wildtype K-RAS and K-RAS^{A59T}, K-RAS^{A59S}, K-RAS^{A59H}, and K-RAS^{A59Y}, at a concentration of 100 μM, were incubated at 37°C for six h with and without 5mM GTP in a reaction buffer containing 50 mM Tris-pH7.5 and 1 mM $MgCl_2$ and analyzed by LC-ESI-MS as previously described (Zhang et al., 2012).

RAS hydrolysis and nucleotide exchange assays—Assays were done with a BioTek microplate reader using black-walled non-TC treated 96-well plates. The GTP hydrolysis assay described here is a modified form of the EnzChek Phosphate Assay Kit assay. For GTP hydrolysis, both preloading of GTP and measurement of inorganic phosphate were done in a 96-well plate format. First, a GTP preloading mixture consisting of 72 μM K-RAS, 10 mM GTP, 4 mM EDTA, and 2 mM DTT in a final volume of 25 μL was stored on ice until use. Second, a GTP hydrolysis mixture consisting of 60 mM Tris, 60 mM NaCl, 6 mM $MgCl_2$, 1.6 mM DTT, 240 μM of 2-amino-6-mercapto-7-methylpurine riboside (MESG), 1.2 U/mL of purine nucleoside phosphorylase (PNP), and varying concentrations of GAP was brought to a final volume of 125 μL. The GTP exchange and reaction mixtures were incubated at 37°C for 35 min in the microplate reader in separate wells in the black-walled 96-well plate. After 35 min, the GTP preloading mixture was added to the hydrolysis mixture and nucleotide hydrolysis was measured over 90 min at 37°C. A change in inorganic phosphate due to GTP hydrolysis was measured by the difference in absorbance at 360nm from a reference reaction without K-RAS protein.

Nucleotide exchange assays were performed for 2’/3′-O-(N-Methyl-anthraniloyl)-guanosine-5′-triphosphate (mant-GTP) or mant-GDP. Mant-GTP and GDP stocks were purchased as 5 mM stocks from Invitrogen. To measure nucleotide exchange at 37°C, we generated a protein mixture containing 1.6 μM K-RAS, 52.5 mM Tris pH 7.5, 52.5 mM NaCl, 5.25 mM $MgCl_2$, 4.2 mM DTT and varying concentrations of SOS1 at a final volume of 140 μL, and a second mixture containing 225 μM of mant-GTP or GDP, 48.6 mM Tris, 48.6 mM NaCl, 4.9 mM $MgCl_2$, 1.9 mM DTT at pH7.5 at a final volume of 10 μL. The two mixtures were placed in the black-walled 96-well plate, wrapped in foil, and incubated in the dark for 30–40 min. Once combined, measurement of nucleotide exchange was taken

every 65 s for 2 h at 37°C. Measurement of mant-nucleotide association with K-RAS was done by excitation at 360nm, detection of fluorescent emission at 440nm, and subtraction of a reference reaction lacking K-RAS protein. Replicate measurements of hydrolysis and nucleotide exchange were used to determine an apparent first-order rate constant (k_{obs}) using the program GraphPad Prism (Notredame et al., 2000).

Measurement of K-RAS^{A59T} in cells and transformation experiments— Measurement of autophosphorylation in response to human Epidermal Growth Factor (hEGF) or insulin signaling was done using SNU-175 cells seeded at a starting density of 7.5×10^5 cells/well in a 6-well plate, allowed to adhere overnight, and then serum starved for 24 h. After serum starvation, induction was done by either addition of vehicle (BSA suspended in HEPES), 1.5 μg/mL of hEGF, or 5 μg/mL of insulin. To measure changes in K-RAS autophosphorylation, cells were lysed at different times in the following manner. First, cells were gently washed once with 1 mL of phosphate buffered saline solution (PBS). Next, 150 μL of radioimmunoprecipitation assay (RIPA) buffer was applied to the well and lysis was allowed to proceed for 15 min at 4°C with gentle rocking. Cell lysate was collected and clarified by high-speed centrifugation at 4°C for 15 min before flash freezing in liquid nitrogen and storage at −80°C. For K-RAS knockdown experiments, shRNA in the pLKO-tet plasmid vector targeting *KRAS*, or GFP as a negative control, was obtained from Addgene and lentivirus was produced as in Ref. (Shao et al., 2014) using HEK293t cells. SNU-175 cells were infected for 24 h and allowed to expand for 1 week before selection with puromycin. For K-RAS knockdown experiments, puromycin selected cells were seeded at a starting density of 5×10^4 cells/well in a 24-well plate. Cells were allowed to adhere overnight before induction of shRNA against *KRAS* using RPMI 1640 media supplemented with 2 μg/mL of doxycycline. To monitor changes in K-RAS autophosphorylation in response to *KRAS* knockdown, cells were lysed every 24 h using the same method as above. To measure the effect of K-RAS knockdown on SNU-175 cell proliferation, parental SNU-175 cells, or cells infected with shRNA suppressing K-RAS or GFP, were grown for 1 week at 2 μg/mL of doxycycline. After one week, 50,000 cells/well were seeded in 24-well plates and allowed to grow for 13 days. A doxycycline positive and negative set of proliferation experiments were performed in parallel.

Ectopic expression of mutant HA-tagged K-RAS4B was done in NIH 3T3 cells using the pBABE-hygro vector and the retroviral pCL packaging system in HEK293t cells (Morgenstern and Land, 1990; Naviaux et al., 1996). First, HEK293t cells were lipofectamine transfected at 70% confluence. On the third day, virus was collected and used to infect NIH 3T3 cells at 20% confluence. Infection proceeded overnight in the TC incubator, and after 48 h, infected cells underwent selection with 300 μg/mL of hygromycin for one week.

Cell lysate for effector binding assays were collected in the following manner. Infected NIH 3T3 cells were grown to high density in 175 mm dishes, and then washed twice with ice-cold 10 mL of PBS and lysed with 400–600μL of MLB solution (25 mM HEPES pH 7.5, 150 mM NaCl, 1% IGEPAL-CA630, 0.25% sodium deoxycholate, 10% glycerol, and 10 mM $MgCl_2$). Lysate and cell debris were immediately scrapped into Eppendorf tubes, rotated for 30 min and then clarified for 30 min using high-speed centrifugation at 4°C.

Cell proliferation was measured over three days at the indicated times at 10% FBS in at least quadruplicate by seeding T25 culture flasks with 5000 cells. Cells were collected and counted using a Nexcelom Bioscience Cellometer® AutoT4 cell counter.

Anchorage independent growth assays were done in triplicate, with quadruplicate repeats, in 12-well plates using only the top and bottom rows. For each well, 2.35×10^4 cells were suspended in 1 mL of soft-agar media (0.83X DMEM, 8.3% FBS, 83 units/mL penicillin, 83 μg/mL of streptomycin, and 0.3% bacto-agar) and carefully placed on top of 1mL of set dense soft-agar (0.67X DMEM, 6.7% FBS, 67 units/mL penicillin, 67μg/mL of streptomycin, and 0.6% bacto-agar). The following day, and every third day after that for three weeks, cells were fed with 250 μL of cell media (1X DMEM, 10%FBS, 100 units/mL penicillin, 100 μg/mL of streptomycin). Colony growth was measured by first carefully removing media from each well, applying 1 mg/mL of MTT dissolved in PBS, and allowing MTT reduction to occur overnight in the TC incubator. The next day, excess solution was removed from each well and plates were scanned using an Epson V600 Photo Scanner. Colonies were counted and analyzed using ImageJ and GraphPad Prism (Notredame et al., 2000; Schneider et al., 2012).

CRISPR mutagenesis of mES cells and related experiments—mES cells with the genotype K-Ras$^{+/LSL\text{-}wildtype}$ were modified using the SaCas9 CRISPR system to be K-Ras$^{A59T/LSL\text{-}A59T}$. The SaCas9 plasmid was modified to contain gRNA sequence targeting exon 2 and codon 59 according to the protocol shown in (Ran et al., 2015). Before nucleofection, mES cells and feeders were washed twice with PBS, and then dissociated by incubation for 10–15 min at 37°C with 0.05% Trypsin-EDTA. Cell solution was collected, excess media was added to inactivate trypsin, and then cells were spun down for 5 min at 4°C at 80xg. Cells were resuspended in media and then applied to a gelatin coated 10 cm dish at 37°C. After 30 min, the non-adherent mES cells were collected and spun down for 5 min at 4°C at 80xg. The cell pellet was resuspended in PBS and cel number was determined using a Nexcelom Bioscience Cellometer® AutoT4 cell counter. Using the same centrifuge conditions, a cell pellet of 3.0×10^6 K-Ras$^{+/LSL\text{-}wildtype}$ mES cells was collected and then redissolved in 90 μL of supplemented nucleofector solution prepared per the Lonza Mouse ES cell Nucleofector® kit protocol. Next, the cell solution was gently mixed with 10 μL of 1X TAE containing 40 μg of single-stranded DNA repair template, purchased from Integrated DNA Technologies, and 5 μg of modified SaCas9 plasmid that was purified from *E.coli* using the PureLink® HiPure Plasmid Filter Maxiprep kit.

Nucleofection was performed according to the Lonza Mouse ES cell Nucleofector® kit protocol. Briefly, the mES cell and DNA solution was carefully added to the supplied cuvette using a plastic pipette. Care was taken to limit air bubbles. The cuvette was then placed in a Nucleofector® II device and the program A-013 was run. Immediately after nucleofection, 500 μL of pre-warmed media was added to the cuvette and gently mixed using the plastic pipette. The entire solution was then added to single well of a gelatin coated 6-well dish with feeders. Cells were fed fresh media every day for 2–3 days. After 2–3 days, cells were collected, diluted 1:1000, and plated on three gelatin coated 10 cm dishes with feeders. The unused cells were spun down at 45C for 5 min at 80xg, resuspended in chilled

mES freezing media (80% media, plus an extra 10% HyColone FBS and 10%DMSO), and then stored for later use at −80°C.

Colonies were grown until visible to the naked eye and then collected in 96-well plates containing 100 μL trypsin/well. After 5–10 min at 37°C, another 100 μL of media was added to each well, cells were resuspended, and then split between two gelatin coated 96-well plates containing feeders. mES clones were then transferred back to 37°C. After 2–4 days, mES clones in one plate were frozen and stored at −80°C by first washing with PBS, dissociating the cells with 50 μL 0.05% trypsin-EDTA for 10 min, and then mixing dissociated cells with 50 μL of 2X mES freezing media (60% media, plus 20% HyClone FBS and 20% DMSO). The other 96-well plate underwent genomic DNA extraction using the *Quick*-DNA kit from Zymo Research.

Besides the A59T mutation, a silent EcoRV restriction site was included in the DNA repair template for genotyping positive mES clones. To genotype clones, 5 μL of extracted genomic DNA was mixed with 0.25 μL of 100 μM of forward and reverse mES Ex2 genotyping primers each, 1 μL of dNTP,10 μL of 5X Phusion HF Buffer, and 0.5 μL of Phusion® High-Fidelity DNA Polymerase. PCR reactions were diluted to a final concentration of 50 μL using Ultrapure water and touchdown PCR, using a melting temperature Tm of 58°C, was performed (Korbie and Mattick, 2008). Once the PCR was complete, 12 μL of the PCR product was removed and mixed with 0.3 mL of EcoRV-HF, 2.5 μL of 10x CutSmart buffer, and 10.2 μL of Ultrapure water. These samples were digested for 1 h at 37°C, enzyme inactivated for 20 min at 65°C, and then run on 1.8%–2.0% TAE agarose gels containing GreenGlo. DNA bands were visualized using a ChemiDoc XRS+ System. Undigested PCR product migrates at ~850 bp, while a positive clone produces a band around ~700 bp. Positive clones were further validated by sequencing using the same PCR recipe, but with the forward and reverse mES Ex2 sequencing primers and a touchdown protocol using a Tm of 56°C. The PCR product was sequenced by Genewiz using the Forward sequencing primer. Finally, K-Ras$^{A59T/LSL\text{-}A59T}$ mES cells were validated at the protein level by detection of an apparently higher migrating band visible by western blot, similar to what we observe in our SNU-175 cells, NIH 3T3 cells, and purified protein.

Detection of MAPK and Akt signaling by western blot was done in mES cells that were expanded in the presence of feeders, but then removed from feeders as above, before being plated in triplicate on gelatin coated dishes. For these experiments mES cells were serum starved for 6 h before lysis.

K-RAS effector binding and precipitation assays—The RAS binding domain of C-RAF kinase (RAF-RBD) (Brtva et al., 1995) and full-length human RASSF5 from the RAS clone collection were obtained from Addgene. The RAS clone collection was a gift from Dominic Esposito (Addgene kit 1000000070). GST tagged RAF1-RBD (GST-RAF-RBD) was expressed and purified from BL21 cells as in ref. (Taylor et al., 2001). GST-tagged RASSF5 (GST-RASSF5) sequence was transferred into the pDEST15 expression vector, and then expressed and purified from BL21-A1 cells. Our protocol for measuring effector-K-RAS interactions was done as in (Taylor et al., 2001), with the following changes. After protein induction, by either isopropyl β-d-1-thiogalactopyranoside (for GST-RAF-RBD) or

arabinose (for GST-RASSF5), cells were washed once in HBS buffer (25 mM HEPES pH 7.5, 150 mM NaCl), resuspended in RLB solution (20 mM HEPES in pH 7.5, 120 mM NaCl, 10% glycerol) and then lysed by sonication. Lysate was clarified by high-speed centrifugation at 4°C, flash frozen and stored at −80°C until use. Before measuring mutant HA-K-RAS4B precipitation by RAF-RBD or RASSF5, HA-K-RAS4B in NIH 3T3 lysates were preloaded with nucleotide by diluting NIH 3T3 lysate in MLB to 2 μg/μL in the presence of 1.0 mg/mL of nucleotide, 15 mM EDTA, and incubated at 32°C for 30 min. After nucleotide preloading, 200 μL of nucleotide exchanged lysate was added to an equal volume of MLB buffer containing 10 μL of GST-RAF1-RBD or GST-RASSF5 loaded glutathione beads. Binding of K-RAS mutants to the different effectors was allowed to proceed for 2 h at 4°C with gentle rotation. After the precipitation reaction was complete, beads were washed three times (> 20,000xg at 4°C) with equal volumes of MLB. The activated state of HA-K-RAS4B in NIH 3T3 cells (i.e., cellular GTP-bound state) was done as above except cell lysates were prepared fresh, not subjected to chemical loading of nucleotide, and precipitation was done in a volume of 300 μL. K-RAS-effector precipitation was detected by western blot and detection of HA-tag. Affinity precipitation of other RASSF proteins was done as above for RASSF5 using plasmids provided by Addgene RAS clone collection (RASSF1: #70535, RASSF2: #70539, RASSF3: #70541, RASSF4: #70543, RASSF6: #70547, RASSF7: #70549, RASSF8: #70551, RASSF9: #70553, RASSF10: #70537).

BRET assay—293FT cells were seeded into 12-well dishes at a concentration of 1×10^5 cells/well. 16 h after plating, pCMV5-Venus-K-Ras4B and pLHCX-CMV-Raf-Rluc8 constructs were transfected into cells using a calcium phosphate protocol (Terrell et al., 2019). Duplicate 12-point saturation curves were generated in which the concentration of the energy donor construct (Rluc8) was held constant (62.5 ng) as the concentration of the energy acceptor plasmid (Venus) increased (0–1.0 μg). 48 h after transfection, cells from each well were collected, washed, and resuspended in PBS (500 μL). 30 μL of the cell suspension was plated in duplicate into wells of a 384-well white-walled plate and coelenterazine-h was added to a final concentration of 3.375 μM. The BRET and Rluc8 emissions were measured simultaneously using a PHERAstar Plus plate reader, with BRET monitored at 535 nm (bandwidth 30 nm) and Rluc8 measured at 475 nm (bandwidth 30 nm). To monitor the increasing levels of acceptor expression, 90 μL of the cell suspension was also plated in duplicate into wells of a 96-well black-walled plate (PerkinElmer OptiPlate), and Venus fluorescence was determined using an excitation wavelength of 485 nm (5 nm bandwidth) and fluorescence read at 530 nm (5 nm bandwidth) using a Tecan Infinite M1000 plate reader. The BRET ratio was determined by calculating the 535/475 ratio for a given sample (sample BRET) and was normalized to the BRET signal from cells expressing the donor construct alone to enable comparisons between experiments. The normalized mBRET signal was calculated as follows: (1000 X (sample BRET ratio/background BRET ratio)) – 1000. The acceptor/donor ratio (Venus emission/Rluc8 emission) for each data point was background corrected and equalized against a control where equal quantities of the Venus (acceptor) and Rluc8 (donor) constructs were transfected to allow for comparisons between experiments. Data was analyzed using GraphPad Prism. Non-linear regression was

used to plot the best fit hyperbolic curve, and values for $BRET_{max}$ and $BRET_{50}$ were obtained from the calculated best fit curves.

Co-immunoprecipitation experiments—HeLa cells were plated at a concentration of 8×10^5 per 10 cm dish 18–24 h prior to transfection. pCMV5-Venus-K-RAS constructs were then transfected into cells using the XtremeGENE9 transfection reagent per the manufacturer's instructions, using a 2:1 ratio of XtremeGENE9 to DNA. 48 h after transfection, serum-starved cells were washed twice with ice cold PBS and lysed in1% NP-40 lysis buffer (20mM Tris [pH 8.0], 137 mM NaCl, 10% glycerol, 1% NP-40 alternative, 0.15 U/mL aprotinin, 1 mM PMSF, 0.5 mM sodium vanadate, 20 μM leupeptin; 500mL/10 cm dish) for 15 min at 4°C on a rocking platform. Lysates were clarified by centrifugation at 14,000 RPM for 10 min at 4°C, after which the protein content was determined by Bradford assays. Lysates containing equivalent amounts of protein were incubated with either anti-GFP/Venus or anti-C-RAF and protein G Sepharose beads for 2 h at 4°C on a rocking platform. Complexes were washed extensively with 1% NP-40 buffer and then examined by western blot analysis along with aliquots of equalized total cell lysate.

Biolayer interferometry—The binding affinities for the RBDs of A-RAF (residues 17–94), B-RAF (residues 150–233), C-RAF (residues 54–137) and the RA domain of RASSF5 (residues 199 –367) of K-RAS-GMPPNP (wild-type, G12V and A59T/E) were measured using an Octet RED-384 biolayer interferometry biosensor instrument (BLI) running Octet Data Acquisition 9.0.0.37 and analyzed with Forté Bio Data analysis software. To prepare GppNHp-loaded K-RAS, protein was incubated in the presence of excess nucleotide analog, EDTA and calf intestinal phosphatase, which were then removed by passage of exchanged protein through size exclusion chromatography (Superdex™ S75 10/300 GL). The RBD/RA of B-RAF, C-RAF, A-RAF and RASSF5 were subcloned into pGEX-4T2 to produce N-terminal GST fusion proteins, which were expressed and purified as described previously (Smith and Ikura, 2014). These GST-tagged proteins were immobilized by incubating anti-GST-conjugated biosensors with GST-RBD proteins (10 μg/mL) for 10 min. The coated sensors were dipped into wells containing a range of concentrations of wild-type K-RAS, $K\text{-}RAS^{G12V}$, $K\text{-}RAS^{A59T}$, or $K\text{-}RAS^{A59E}$ (54.7 nM to 20 μM K-RAS) in 20 mM HEPES, 100 mM NaCl, 5 mM $MgCl_2$, 2 mM TCEP, 0.01% BSA and 0.005% Tween-20) for 30 or 60 s to monitor association, then transferred to buffer alone to monitor dissociation for 30 or 60 s. These binding assays were performed at 25°C in 96-well plates with agitation (1000 RPM). Analogous experiments were performed using GST-RASSF5-RA (immobilized at 5 μg/mL) with K-RAS concentrations ranging from 62 nM to 50 μM K-RAS. Sensors with immobilized GST-RBD/RAs were dipped into buffer alone as a control. Binding data were fitted to a 1:1 binding stoichiometry model using both kinetic and steady state analyses. GraphPad 9.1.0 was used to perform t tests and prepare graphs.

Western blotting and antibodies—All samples were run on either homemade 12.5% polyacrylamide gels or criterion pre-cast TGX gels from Bio-Rad. Wet transfer was performed overnight at 20V and at 4°C. Membranes were blocked for 1 h at room temp, with gentle agitation, using Intercept TBS buffer. Primary antibodies were diluted in Intercept T20 antibody diluent buffer, per manufacturer protocol, and precipitation was

allowed to proceed overnight at 4°C with gentle agitation. The following day, blots were washed 3–4 times at room temperature in 5–15 min intervals using homemade 1X TBST, before the addition of secondary antibodies dissolved in Intercept T20 antibody diluent buffer. Secondary precipitation was allowed to proceed for 1 h at room temperature with gentle agitation. Blots were again washed 3–4 times at room temperature in 5–15 min intervals using homemade 1X TBST. Western blot bands were visualized and quantified using a Li-COR Biosciences imaging system.

The antibodies used in experiments involving the SNU-175, mES and NIH 3T3 cell lines are as follows: anti-GST (Cell Signaling Technologies, 2625), anti-HA-tag (Cell Signaling Technologies, 2367), pC-Raf (Cell Signaling Technologies, 9431), phospho-MEK1/2 (Cell Signaling Technologies, 9121), polyclonal KRAS antibody (Proteintech, 12063–1-AP), RAS10 (Millipore-Sigma, 05–516), vinculin (Cell Signaling Technologies, 13901), p44/42 MAPK (Erk1/2) (Cell Signaling Technologies, 4696), phospho-p44/42 MAPK (Erk1/2) (Cell Signaling Technologies, 4377), MEK1/2 (Cell Signaling Technologies, 4694), phospho-MEK1/2 (Cell Signaling Technologies, 9154), Akt (Cell Signaling Technologies, 2920), phospho-Akt (Cell Signaling Technologies, 4060), S6 ribosomal protein (Cell Signaling Technologies, 2317), phospho-S6 ribosomal protein (Cell Signaling Technologies, 2211), and C-Raf (Cell Signaling Technologies, 12552S).

The antibodies used in the co-immunoprecipitation experiments are as follows: A-Raf (Santa Cruz, sc-408), B-Raf (Santa Cruz, sc-5284), C-Raf (BD Pharmagen, 610152), GFP (MBL International, D153–3), Venus (Roche, 118114460001), MEK1 (BD Biosciences, 610122), and phospho-MEK1/2 (Cell Signaling Technologies, 9121).

QUANTIFICATION AND STATISTICAL ANALYSIS

No statistical methods were used to predetermine sample size. The experiments were not randomized, nor were investigators blinded to sample allocation and experimental assessment. For biochemical or enzymology experiments, t tests were used to determine significance. For biological experiments, the Mann-Whitney U-test was used to determine significance, unless otherwise indicated.

Supplementary Material

Refer to Web version on PubMed Central for supplementary material.

ACKNOWLEDGMENTS

This work was supported by grants from the NIH (R01CA178017 and R01CA232372 to K.M.H.) and an award from the Cancer Research UK Grand Challenge and the Mark Foundation to the SPECIFICANCER team. C.W.J. was supported by postdoctoral fellowship 130428-PF-17-066-01-TBG from ACS. S.D.P. acknowledges funding from the Linde Family Foundation, the Doris Duke Charitable Foundation, Deerfield 3DC, and Taiho Pharmaceuticals. Work from the Princess Margaret Cancer Centre was supported by the Canadian Cancer Society Research Institute (Grant # 706696 to M.I.) and the Princess Margaret Cancer Foundation. The NMR spectrometer and Octet biosensor were funded by CFI. Work done at the NCI was supported by federal funds from the NCI (ZIA BC 010329). Synchrotron data collection was done at the Northeastern Collaborative Access Team beamlines, which were funded by the NIGMS from the NIH (P30 GM124165). The Eiger 16M detector on the 24-ID-E beam line was funded by a NIH-ORIP HEI grant (S10OD021527). This research used resources of the Advanced Photon Source, a DOE Office of Science User Facility at Argonne National Laboratory under Contract No. DE-AC02-06CH11357. The MicroMax007HF used to collect the X-ray data at Northeastern University was purchased

in part with funds from the NSF MRI-1228897 grant to C.M. We thank Isidoro Tavares and Scott Ficarro from the Blais Proteomics Center for conducting mass spectrometry analyses. Molecular dynamics simulations were conducted on the HMS O2 High Performance Compute Cluster (https://it.hms.harvard.edu/our-services/research-computing).

REFERENCES

Abraham MJ, Murtola T, Schulz R, Páll S, Smith JC, Hess B, and Lindahl E. (2015). GROMACS: High performance molecular simulations through multi-level parallelism from laptops to supercomputers. SoftwareX 1-2, 19–25.

Adams PD, Afonine PV, Bunkóczi G, Chen VB, Davis IW, Echols N, Headd JJ, Hung LW, Kapral GJ, Grosse-Kunstleve RW, et al. (2010). PHENIX: a comprehensive Python-based system for macromolecular structure solution. Acta Crystallogr. D Biol. Crystallogr 66, 213–221. [PubMed: 20124702]

Ahearn I, Zhou M, and Philips MR (2018). Posttranslational Modifications of RAS Proteins. Cold Spring Harb. Perspect. Med 8, a031484.

Barthelmes K, Ramcke E, Kang HS, Sattler M, and Itzen A. (2020). Conformational control of small GTPases by AMPylation. Proc. Natl. Acad. Sci. USA 117, 5772–5781. [PubMed: 32123090]

Bergom C, Hauser AD, Rymaszewski A, Gonyo P, Prokop JW, Jennings BC, Lawton AJ, Frei A, Lorimer EL, Aguilera-Barrantes I, et al. (2016). The tumor-suppressive small GTPase DiRas1 binds the noncanonical guanine nucleotide exchange factor SmgGDS and antagonizes SmgGDS interactions with oncogenic small GTPases. J. Biol. Chem 291, 10948. [PubMed: 27197236]

Boriack-Sjodin PA, Margarit SM, Bar-Sagi D, and Kuriyan J. (1998). The structural basis of the activation of Ras by Sos. Nature 394, 337–343. [PubMed: 9690470]

Bouchard-Cannon P, Lowden C, Trinh D, and Cheng HM (2018). Dexras1 is a homeostatic regulator of exercise-dependent proliferation and cell survival in the hippocampal neurogenic niche. Sci. Rep 8, 5294. [PubMed: 29593295]

Boute N, Jockers R, and Issad T. (2002). The use of resonance energy transfer in high-throughput screening: BRET versus FRET. Trends Pharmacol. Sci 23, 351–354. [PubMed: 12377570]

Brooks BR, Brooks CL 3rd, Mackerell AD Jr., Nilsson L, Petrella RJ, Roux B, Won Y, Archontis G, Bartels C, Boresch S, et al. (2009). CHARMM: the biomolecular simulation program. J. Comput. Chem 30, 1545–1614. [PubMed: 19444816]

Brtva TR, Drugan JK, Ghosh S, Terrell RS, Campbell-Burk S, Bell RM, and Der CJ (1995). Two distinct Raf domains mediate interaction with Ras. J. Biol. Chem 270, 9809–9812. [PubMed: 7730360]

Buhrman G, Holzapfel G, Fetics S, and Mattos C. (2010). Allosteric modulation of Ras positions Q61 for a direct role in catalysis. Proc. Natl. Acad. Sci. USA 107, 4931–4936. [PubMed: 20194776]

Castel P, Dharmaiah S, Sale MJ, Messing S, Rizzuto G, Cuevas-Navarro A, Cheng A, Trnka MJ, Urisman A, Esposito D, et al. (2021). RAS interaction with Sin1 is dispensable for mTORC2 assembly and activity. Proc. Natl. Acad. Sci. USA 118, e2103261118.

Castellano E, and Downward J. (2011). RAS Interaction with PI3K: More Than Just Another Effector Pathway. Genes Cancer 2, 261–274. [PubMed: 21779497]

Cha JY, Kim HJ, Yu JH, Xu J, Kim D, Paul BD, Choi H, Kim S, Lee YJ, Ho GP, et al. (2013). Dexras1 mediates glucocorticoid-associated adipogenesis and diet-induced obesity. Proc. Natl. Acad. Sci. USA 110, 20575–20580. [PubMed: 24297897]

Cheng HY, Obrietan K, Cain SW, Lee BY, Agostino PV, Joza NA, Harrington ME, Ralph MR, and Penninger JM (2004). Dexras1 potentiates photic and suppresses nonphotic responses of the circadian clock. Neuron 43, 715–728. [PubMed: 15339652]

Cherfils J, and Zeghouf M. (2013). Regulation of small GTPases by GEFs, GAPs, and GDIs. Physiol. Rev 93, 269–309. [PubMed: 23303910]

Chung HH, Benson DR, and Schultz PG (1993). Probing the structure and mechanism of Ras protein with an expanded genetic code. Science 259, 806–809. [PubMed: 8430333]

Cookis T, and Mattos C. (2021). Crystal Structure Reveals the Full Ras-Raf Interface and Advances Mechanistic Understanding of Raf Activation. Biomolecules 11, 996. [PubMed: 34356620]

Cool RH, Jensen M, Jonák J, Clark BF, and Parmeggiani A. (1990). Substitution of proline 82 by threonine induces autophosphorylating activity in GTP-binding domain of elongation factor Tu. J. Biol. Chem 265, 6744–6749. [PubMed: 2157708]

Coordinators NR; NCBI Resource Coordinators (2016). Database resources of the National Center for Biotechnology Information. Nucleic Acids Res. 44 (D1), D7–D19. [PubMed: 26615191]

Dart AE, Box GM, Court W, Gale ME, Brown JP, Pinder SE, Eccles SA, and Wells CM (2015). PAK4 promotes kinase-independent stabilization of RhoU to modulate cell adhesion. J. Cell Biol 211, 863–879. [PubMed: 26598620]

Daura X, Gademann K, Jaun B, Seebach D, van Gunsteren WF, and Mark AE (1999). Peptide Folding: When Simulation Meets Experiment. Angew. Chem. Int. Ed. Engl 38, 236–240.

Delaglio F, Grzesiek S, Vuister GW, Zhu G, Pfeifer J, and Bax A. (1995). NMRPipe: a multidimensional spectral processing system based on UNIX pipes. J. Biomol. NMR 6, 277–293. [PubMed: 8520220]

Dhanaraman T, Singh S, Killoran RC, Singh A, Xu X, Shifman JM, and Smith MJ (2020). RASSF effectors couple diverse RAS subfamily GTPases to the Hippo pathway. Sci. Signal 13, eabb4778.

Dharmaiah S, Bindu L, Tran TH, Gillette WK, Frank PH, Ghirlando R, Nissley DV, Esposito D, McCormick F, Stephen AG, and Simanshu DK (2016). Structural basis of recognition of farnesylated and methylated KRAS4b by PDEδ. Proc. Natl. Acad. Sci. USA 113, E6766–E6775. [PubMed: 27791178]

Dharmaiah S, Tran TH, Messing S, Agamasu C, Gillette WK, Yan W, Waybright T, Alexander P, Esposito D, Nissley DV, et al. (2019). Structures of N-terminally processed KRAS provide insight into the role of N-acetylation. Sci. Rep 9, 10512. [PubMed: 31324887]

Donninger H, Schmidt ML, Mezzanotte J, Barnoud T, and Clark GJ (2016). Ras signaling through RASSF proteins. Semin. Cell Dev. Biol 58, 86–95. [PubMed: 27288568]

Dougherty MK, Müller J, Ritt DA, Zhou M, Zhou XZ, Copeland TD, Conrads TP, Veenstra TD, Lu KP, and Morrison DK (2005). Regulation of Raf-1 by direct feedback phosphorylation. Mol. Cell 17, 215–224. [PubMed: 15664191]

Elias JE, and Gygi SP (2007). Target-decoy search strategy for increased confidence in large-scale protein identifications by mass spectrometry. Nat. Methods 4, 207–214. [PubMed: 17327847]

Emsley P, and Cowtan K. (2004). Coot: model-building tools for molecular graphics. Acta Crystallogr. D Biol Crystallogr. 60, 2126–2132.

Eng JK, McCormack AL, and Yates JR (1994). An approach to correlate tandem mass spectral data of peptides with amino acid sequences in a protein database. J. Am. Soc. Mass Spectrom 5, 976–989. [PubMed: 24226387]

Fan Y, Esmail MA, Ansley SJ, Blacque OE, Boroevich K, Ross AJ, Moore SJ, Badano JL, May-Simera H, Compton DS, et al. (2004). Mutations in a member of the Ras superfamily of small GTP-binding proteins causes Bardet-Biedl syndrome. Nat. Genet 36, 989–993. [PubMed: 15314642]

Fang Z, Lee KY, Huo KG, Gasmi-Seabrook G, Zheng L, Moghal N, Tsao MS, Ikura M, and Marshall CB (2020). Multivalent assembly of KRAS with the RAS-binding and cysteine-rich domains of CRAF on the membrane. Proc. Natl. Acad. Sci. USA 117, 12101–12108. [PubMed: 32414921]

Fetics SK, Guterres H, Kearney BM, Buhrman G, Ma B, Nussinov R, and Mattos C. (2015). Allosteric effects of the oncogenic RasQ61L mutant on Raf-RBD. Structure 23, 505–516. [PubMed: 25684575]

Feuerstein J, Goody RS, and Wittinghofer A. (1987). Preparation and characterization of nucleotide-free and metal ion-free p21 “apoprotein”. J. Biol. Chem 262, 8455–8458. [PubMed: 3298232]

Fiegen D, Blumenstein L, Stege P, Vetter IR, and Ahmadian MR (2002). Crystal structure of Rnd3/RhoE: functional implications. FEBS Lett. 525, 100–104. [PubMed: 12163169]

Foster R, Hu KQ, Lu Y, Nolan KM, Thissen J, and Settleman J. (1996). Identification of a novel human Rho protein with unusual properties: GTPase deficiency and in vivo farnesylation. Mol. Cell. Biol 16, 2689–2699. [PubMed: 8649376]

Frech M, Schlichting I, Wittinghofer A, and Chardin P. (1990). Guanine nucleotide binding properties of the mammalian RalA protein produced in Escherichia coli. J. Biol. Chem 265, 6353–6359. [PubMed: 2108160]

Freeman AK, Ritt DA, and Morrison DK (2013). Effects of Raf dimerization and its inhibition on normal and disease-associated Raf signaling. Mol. Cell 49, 751–758. [PubMed: 23352452]

Gasper R, Sot B, and Wittinghofer A. (2010). GTPase activity of Di-Ras proteins is stimulated by Rap1GAP proteins. Small GTPases 1, 133–141. [PubMed: 21686267]

Ghiglieri V, Napolitano F, Pelosi B, Schepisi C, Migliarini S, Di Maio A, Pendolino V, Mancini M, Sciamanna G, Vitucci D, et al. (2015). Rhes influences striatal cAMP/PKA-dependent signaling and synaptic plasticity in a gender-sensitive fashion. Sci. Rep 5, 10933. [PubMed: 26190541]

Gibbs JB, Ellis RW, and Scolnick EM (1984). Autophosphorylation of v-Ha-ras p21 is modulated by amino acid residue 12. Proc. Natl. Acad. Sci. USA 81, 2674–2678. [PubMed: 6609366]

Haigis KM (2017). KRAS Alleles: The Devil Is in the Detail. Trends Cancer 3, 686–697. [PubMed: 28958387]

Hall BE, Yang SS, Boriack-Sjodin PA, Kuriyan J, and Bar-Sagi D. (2001). Structure-based mutagenesis reveals distinct functions for Ras switch 1 and switch 2 in Sos-catalyzed guanine nucleotide exchange. J. Biol. Chem 276, 27629–27637. [PubMed: 11333268]

Hamad NM, Elconin JH, Karnoub AE, Bai W, Rich JN, Abraham RT, Der CJ, and Counter CM (2002). Distinct requirements for Ras oncogenesis in human versus mouse cells. Genes Dev. 16, 2045–2057. [PubMed: 12183360]

Hancock JF, Cadwallader K, and Marshall CJ (1991). Methylation and proteolysis are essential for efficient membrane binding of prenylated p21K-ras(B). EMBO J. 10, 641–646. [PubMed: 2001678]

Heng JI, Nguyen L, Castro DS, Zimmer C, Wildner H, Armant O, Skowronska-Krawczyk D, Bedogni F, Matter JM, Hevner R, and Guillemot F. (2008). Neurogenin 2 controls cortical neuron migration through regulation of Rnd2. Nature 455, 114–118. [PubMed: 18690213]

Hobbs GA, Baker NM, Miermont AM, Thurman RD, Pierobon M, Tran TH, Anderson AO, Waters AM, Diehl JN, Papke B, et al. (2020). Atypical $KRAS^{G12R}$ Mutant Is Impaired in PI3K Signaling and Macropinocytosis in Pancreatic Cancer. Cancer Discov. 10, 104–123. [PubMed: 31649109]

Humphrey W, Dalke A, and Schulten K. (1996). VMD: visual molecular dynamics. J. Mol. Graph 14, 33–38, 27–28. [PubMed: 8744570]

Hunter JC, Gurbani D, Ficarro SB, Carrasco MA, Lim SM, Choi HG, Xie T, Marto JA, Chen Z, Gray NS, and Westover KD (2014). In situ selectivity profiling and crystal structure of SML-8–73-1, an active site inhibitor of oncogenic K-Ras G12C. Proc. Natl. Acad. Sci. USA 111, 8895–8900. [PubMed: 24889603]

Jacob A, Linklater E, Bayless BA, Lyons T, and Prekeris R. (2016). The role and regulation of Rab40b-Tks5 complex during invadopodia formation and cancer cell invasion. J. Cell Sci 129, 4341–4353. [PubMed: 27789576]

Jo S, Kim T, Iyer VG, and Im W. (2008). CHARMM-GUI: a web-based graphical user interface for CHARMM. J. Comput. Chem 29, 1859–1865. [PubMed: 18351591]

John J, Frech M, and Wittinghofer A. (1988). Biochemical properties of Ha-ras encoded p21 mutants and mechanism of the autophosphorylation reaction. J. Biol. Chem 263, 11792–11799. [PubMed: 3042780]

Johnson CW, Buhrman G, Ting PY, Colicelli J, and Mattos C. (2015). Expression, purification, crystallization and X-ray data collection for RAS and its mutants. Data Brief 6, 423–427. [PubMed: 26866052]

Johnson CW, Lin YJ, Reid D, Parker J, Pavlopoulos S, Dischinger P, Graveel C, Aguirre AJ, Steensma M, Haigis KM, and Mattos C. (2019). Isoform-Specific Destabilization of the Active Site Reveals a Molecular Mechanism of Intrinsic Activation of KRas G13D. Cell Rep. 28, 1538–1550.e7. [PubMed: 31390567]

Kabsch W. (2010). Integration, scaling, space-group assignment and post-refinement. Acta Crystallogr. D Biol. Crystallogr 66, 133–144. [PubMed: 20124693]

Kano Y, Gebregiworgis T, Marshall CB, Radulovich N, Poon BPK, St-Germain J, Cook JD, Valencia-Sama I, Grant BMM, Herrera SG, et al. (2019). Tyrosyl phosphorylation of KRAS stalls GTPase cycle via alteration of switch I and II conformation. Nat. Commun 10, 224. [PubMed: 30644389]

Kemppainen RJ, and Behrend EN (1998). Dexamethasone rapidly induces a novel ras superfamily member-related gene in AtT-20 cells. J. Biol. Chem 273, 3129–3131. [PubMed: 9452419]

Khokhlatchev A, Rabizadeh S, Xavier R, Nedwidek M, Chen T, Zhang XF, Seed B, and Avruch J. (2002). Identification of a novel Ras-regulated proapoptotic pathway. Curr. Biol 12, 253–265. [PubMed: 11864565]

Klink BU, and Scheidig AJ (2010). New insight into the dynamic properties and the active site architecture of H-Ras p21 revealed by X-ray crystallography at very high resolution. BMC Struct. Biol 10, 38. [PubMed: 20973973]

Kobayashi T, Hori Y, Ueda N, Kajiho H, Muraoka S, Shima F, Kataoka T, Kontani K, and Katada T. (2009). Biochemical characterization of missense mutations in the Arf/Arl-family small GTPase Arl6 causing Bardet-Biedl syndrome. Biochem. Biophys. Res. Commun 381, 439–442. [PubMed: 19236846]

Kontani K, Tada M, Ogawa T, Okai T, Saito K, Araki Y, and Katada T. (2002). Di-Ras, a distinct subgroup of ras family GTPases with unique biochemical properties. J. Biol. Chem 277, 41070–41078. [PubMed: 12194967]

Korbie DJ, and Mattick JS (2008). Touchdown PCR for increased specificity and sensitivity in PCR amplification. Nat. Protoc 3, 1452–1456. [PubMed: 18772872]

Kovalski JR, Bhaduri A, Zehnder AM, Neela PH, Che Y, Wozniak GG, and Khavari PA (2019). The Functional Proximal Proteome of Oncogenic Ras Includes mTORC2. Mol Cell 73, 830–844.e812. [PubMed: 30639242]

Krengel U, Schlichting I, Scherer A, Schumann R, Frech M, John J, Kabsch W, Pai EF, and Wittinghofer A. (1990). Three-dimensional structures of H-ras p21 mutants: molecular basis for their inability to function as signal switch molecules. Cell 62, 539–548. [PubMed: 2199064]

Ku JL, and Park JG (2005). Biology of SNU cell lines. Cancer Res. Treat 37, 1–19. [PubMed: 19956504]

Lee RH, Iioka H, Ohashi M, Iemura S, Natsume T, and Kinoshita N. (2007). XRab40 and XCullin5 form a ubiquitin ligase complex essential for the noncanonical Wnt pathway. EMBO J. 26, 3592–3606. [PubMed: 17627283]

Lee J, Cheng X, Swails JM, Yeom MS, Eastman PK, Lemkul JA, Wei S, Buckner J, Jeong JC, Qi Y, et al. (2016). CHARMM-GUI Input Generator for NAMD, GROMACS, AMBER, OpenMM, and CHARMM/OpenMM Simulations Using the CHARMM36 Additive Force Field. J. Chem. Theory Comput 12, 405–413. [PubMed: 26631602]

Li Y, Jia Q, Wang Y, Li F, Jia Z, and Wan Y. (2015). Rab40b upregulation correlates with the prognosis of gastric cancer by promoting migration, invasion, and metastasis. Med. Oncol 32, 126. [PubMed: 25790780]

Li C, Vides A, Kim D, Xue JY, Zhao Y, and Lito P. (2021). The G protein signaling regulator RGS3 enhances the GTPase activity of KRAS. Science 374, 197–201. [PubMed: 34618566]

Lu J, Bera AK, Gondi S, and Westover KD (2018). KRAS Switch Mutants D33E and A59G Crystallize in the State 1 Conformation. Biochemistry 57, 324–333. [PubMed: 29235861]

Luo X, Li C, Tan R, Xu X, Wu WKK, Satoh A, Wang T, and Yu S. (2017). A RasGAP, DAB2IP, regulates lipid droplet homeostasis by serving as GAP toward RAB40C. Oncotarget 8, 85415–85427. [PubMed: 29156729]

Maurer T, Garrenton LS, Oh A, Pitts K, Anderson DJ, Skelton NJ, Fauber BP, Pan B, Malek S, Stokoe D, et al. (2012). Small-molecule ligands bind to a distinct pocket in Ras and inhibit SOS-mediated nucleotide exchange activity. Proc. Natl. Acad. Sci. USA 109, 5299–5304. [PubMed: 22431598]

McCoy AJ, Grosse-Kunstleve RW, Adams PD, Winn MD, Storoni LC, and Read RJ (2007). Phaser crystallographic software. J. Appl. Cryst 40, 658–674. [PubMed: 19461840]

Morgenstern JP, and Land H. (1990). Advanced mammalian gene transfer: high titre retroviral vectors with multiple drug selection markers and a complementary helper-free packaging cell line. Nucleic Acids Res. 18, 3587–3596. [PubMed: 2194165]

Mouly L, Gilhodes J, Lemarié A, Cohen-Jonathan Moyal E, Toulas C, Favre G, Sordet O, and Monferran S. (2019). The RND1 Small GTPase: Main Functions and Emerging Role in Oncogenesis. Int. J. Mol. Sci 20, 3612.

Nachury MV (2018). The molecular machines that traffic signaling receptors into and out of cilia. Curr. Opin. Cell Biol 51, 124–131. [PubMed: 29579578]

Napolitano F, D'Angelo L, de Girolamo P, Avallone L, de Lange P, and Usiello A. (2018). The Thyroid Hormone-target Gene Rhes a Novel Crossroad for Neurological and Psychiatric Disorders: New Insights from Animal Models. Neuroscience 384, 419–428. [PubMed: 29857029]

Naviaux RK, Costanzi E, Haas M, and Verma IM (1996). The pCL vector system: rapid production of helper-free, high-titer, recombinant retroviruses. J. Virol 70, 5701–5705. [PubMed: 8764092]

Nobes CD, Lauritzen I, Mattei MG, Paris S, Hall A, and Chardin P. (1998). A new member of the Rho family, Rnd1, promotes disassembly of actin filament structures and loss of cell adhesion. J. Cell Biol 141, 187–197. [PubMed: 9531558]

Notredame C, Higgins DG, and Heringa J. (2000). T-Coffee: A novel method for fast and accurate multiple sequence alignment. J. Mol. Biol 302, 205–217. [PubMed: 10964570]

Ogita Y, Egami S, Ebihara A, Ueda N, Katada T, and Kontani K. (2015). Di-Ras2 Protein Forms a Complex with SmgGDS Protein in Brain Cytosol in Order to Be in a Low Affinity State for Guanine Nucleotides. J. Biol. Chem 290, 20245–20256. [PubMed: 26149690]

Oh JH, Ku JL, Yoon KA, Kwon HJ, Kim WH, Park HS, Yeo KS, Song SY, Chung JK, and Park JG (1999). Establishment and characterization of 12 human colorectal-carcinoma cell lines. Int. J. Cancer 81, 902–910. [PubMed: 10362137]

Okada T, Sinha S, Esposito I, Schiavon G, López-Lago MA, Su W, Pratilas CA, Abele C, Hernandez JM, Ohara M, et al. (2015). The Rho GTPase Rnd1 suppresses mammary tumorigenesis and EMT by restraining Ras-MAPK signalling. Nat. Cell Biol 17, 81–94. [PubMed: 25531777]

Otwinowski Z, and Minor W. (1997). Processing of X-ray diffraction data collected in oscillation mode. Methods Enzymol. 276, 307–326.

Pacold ME, Suire S, Perisic O, Lara-Gonzalez S, Davis CT, Walker EH, Hawkins PT, Stephens L, Eccleston JF, and Williams RL (2000). Crystal structure and functional analysis of Ras binding to its effector phosphoinositide 3-kinase gamma. Cell 103, 931–943. [PubMed: 11136978]

Parker JA, Volmar AY, Pavlopoulos S, and Mattos C. (2018). K-Ras Populates Conformational States Differently from Its Isoform H-Ras and Oncogenic Mutant K-RasG12D. Structure 26, 810–820.e814.

Paysan L, Piquet L, Saltel F, and Moreau V. (2016). Rnd3 in Cancer: A Review of the Evidence for Tumor Promoter or Suppressor. Mol. Cancer Res 14, 1033–1044. [PubMed: 27555595]

Peng J, Schwartz D, Elias JE, Thoreen CC, Cheng D, Marsischky G, Roelofs J, Finley D, and Gygi SP (2003). A proteomics approach to understanding protein ubiquitination. Nat. Biotechnol 21, 921–926. [PubMed: 12872131]

Pettersen EF, Goddard TD, Huang CC, Couch GS, Greenblatt DM, Meng EC, and Ferrin TE (2004). UCSF Chimera–a visualization system for exploratory research and analysis. J. Comput. Chem 25, 1605–1612. [PubMed: 15264254]

Poulin EJ, Bera AK, Lu J, Lin YJ, Strasser SD, Paulo JA, Huang TQ, Morales C, Yan W, Cook J, et al. (2019). Tissue-Specific Oncogenic Activity of $KRAS^{A146T}$. Cancer Discov. 9, 738–755. [PubMed: 30952657]

Qu L, Pan C, He SM, Lang B, Gao GD, Wang XL, and Wang Y. (2019). The Ras Superfamily of Small GTPases in Non-neoplastic Cerebral Diseases. Front. Mol. Neurosci 12, 121. [PubMed: 31213978]

Ran FA, Cong L, Yan WX, Scott DA, Gootenberg JS, Kriz AJ, Zetsche B, Shalem O, Wu X, Makarova KS, et al. (2015). In vivo genome editing using Staphylococcus aureus Cas9. Nature 520, 186–191. [PubMed: 25830891]

Reif A, Nguyen TT, Weissflog L, Jacob CP, Romanos M, Renner TJ, Buttenschon HN, Kittel-Schneider S, Gessner A, Weber H, et al. (2011). DIRAS2 is associated with adult ADHD, related traits, and co-morbid disorders. Neuropsychopharmacology 36, 2318–2327. [PubMed: 21750579]

Riou P, Villalonga P, and Ridley AJ (2010). Rnd proteins: multifunctional regulators of the cytoskeleton and cell cycle progression. BioEssays 32, 986–992. [PubMed: 20836090]

Rodriguez-Gabin AG, Almazan G, and Larocca JN (2004). Vesicle transport in oligodendrocytes: probable role of Rab40c protein. J. Neurosci. Res 76, 758–770. [PubMed: 15160388]

Sasaki AT, Carracedo A, Locasale JW, Anastasiou D, Takeuchi K, Kahoud ER, Haviv S, Asara JM, Pandolfi PP, and Cantley LC (2011). Ubiquitination of K-Ras enhances activation and facilitates binding to select downstream effectors. Sci. Signal 4, ra13.

Scheffzek K, Ahmadian MR, Kabsch W, Wiesmu€ller L, Lautwein A, Schmitz F, and Wittinghofer A. (1997). The Ras-RasGAP complex: structural basis for GTPase activation and its loss in oncogenic Ras mutants. Science 277, 333–338. [PubMed: 9219684]

Scheidig AJ, Burmester C, and Goody RS (1999). The pre-hydrolysis state of p21(ras) in complex with GTP: new insights into the role of water molecules in the GTP hydrolysis reaction of ras-like proteins. Structure 7, 1311–1324. [PubMed: 10574788]

Schneider CA, Rasband WS, and Eliceiri KW (2012). NIH Image to ImageJ: 25 years of image analysis. Nat. Methods 9, 671–675. [PubMed: 22930834]

Shahani N, Swarnkar S, Giovinazzo V, Morgenweck J, Bohn LM, Scharager-Tapia C, Pascal B, Martinez-Acedo P, Khare K, and Subramaniam S. (2016). RasGRP1 promotes amphetamine-induced motor behavior through a Rhes interaction network ("Rhesactome") in the striatum. Sci. Signal 9, ra111.

Shao DD, Xue W, Krall EB, Bhutkar A, Piccioni F, Wang X, Schinzel AC, Sood S, Rosenbluh J, Kim JW, et al. (2014). KRAS and YAP1 converge to regulate EMT and tumor survival. Cell 158, 171–184. [PubMed: 24954536]

Sharma M, Ramírez Jarquín UN, Rivera O, Kazantzis M, Eshraghi M, Shahani N, Sharma V, Tapia R, and Subramaniam S. (2019). Rhes, a striatal-enriched protein, promotes mitophagy via Nix. Proc. Natl. Acad. Sci. USA 116, 23760–23771. [PubMed: 31676548]

Shih TY, Papageorge AG, Stokes PE, Weeks MO, and Scolnick EM (1980). Guanine nucleotide-binding and autophosphorylating activities associated with the p21src protein of Harvey murine sarcoma virus. Nature 287, 686–691. [PubMed: 6253810]

Simanshu DK, Nissley DV, and McCormick F. (2017). RAS Proteins and Their Regulators in Human Disease. Cell 170, 17–33. [PubMed: 28666118]

Smith MJ, and Ikura M. (2014). Integrated RAS signaling defined by parallel NMR detection of effectors and regulators. Nat. Chem. Biol 10, 223–230. [PubMed: 24441586]

Spoerner M, Herrmann C, Vetter IR, Kalbitzer HR, and Wittinghofer A. (2001). Dynamic properties of the Ras switch I region and its importance for binding to effectors. Proc. Natl. Acad. Sci. USA 98, 4944–4949. [PubMed: 11320243]

Stieglitz B, Bee C, Schwarz D, Yildiz O, Moshnikova A, Khokhlatchev A, and Herrmann C. (2008). Novel type of Ras effector interaction established between tumour suppressor NORE1A and Ras switch II. EMBO J. 27, 1995–2005. [PubMed: 18596699]

Sutton MN, Yang H, Huang GY, Fu C, Pontikos M, Wang Y, Mao W, Pang L, Yang M, Liu J, et al. (2018). RAS-related GTPases DIRAS1 and DIRAS2 induce autophagic cancer cell death and are required for autophagy in murine ovarian cancer cells. Autophagy 14, 637–653. [PubMed: 29368982]

Swarnkar S, Chen Y, Pryor WM, Shahani N, Page DT, and Subramaniam S. (2015). Ectopic expression of the striatal-enriched GTPase Rhes elicits cerebellar degeneration and an ataxia phenotype in Huntington's disease. Neurobiol. Dis 82, 66–77. [PubMed: 26048156]

Tang YJ, Huang J, Tsushima H, Ban GI, Zhang H, Oristian KM, Puviindran V, Williams N, Ding X, Ou J, et al. (2019). Tracing Tumor Evolution in Sarcoma Reveals Clonal Origin of Advanced Metastasis. Cell Rep 28, 2837–2850.e2835. [PubMed: 31509746]

Tate JG, Bamford S, Jubb HC, Sondka Z, Beare DM, Bindal N, Boutselakis H, Cole CG, Creatore C, Dawson E, et al. (2019). COSMIC: the Catalogue Of Somatic Mutations In Cancer. Nucleic Acids Res. 47 (D1), D941–D947. [PubMed: 30371878]

Taylor SJ, Resnick RJ, and Shalloway D. (2001). Nonradioactive determination of Ras-GTP levels using activated ras interaction assay. Methods Enzymol. 333, 333–342. [PubMed: 11400349]

Terrell EM, Durrant DE, Ritt DA, Sealover NE, Sheffels E, Spencer-Smith R, Esposito D, Zhou Y, Hancock JF, Kortum RL, et al. (2019). Distinct Binding Preferences between Ras and Raf Family Members and the Impact on Oncogenic Ras Signaling. Mol Cell 76, 872–884.e875. [PubMed: 31606273]

Ting PY, Johnson CW, Fang C, Cao X, Graeber TG, Mattos C, and Colicelli J. (2015). Tyrosine phosphorylation of RAS by ABL allosterically enhances effector binding. FASEB J. 29, 3750–3761. [PubMed: 25999467]

Touchot N, Zahraoui A, Vielh E, and Tavitian A. (1989). Biochemical properties of the YPT-related rab1B protein. Comparison with rab1A. FEBS Lett. 256, 79–84. [PubMed: 2509243]

Tran TH, Chan AH, Young LC, Bindu L, Neale C, Messing S, Dharmaiah S, Taylor T, Denson JP, Esposito D, et al. (2021). KRAS interaction with RAF1 RAS-binding domain and cysteine-rich domain provides insights into RAS-mediated RAF activation. Nat. Commun 12, 1176. [PubMed: 33608534]

Ulsh LS, and Shih TY (1984). Metabolic turnover of human c-rasH p21 protein of EJ bladder carcinoma and its normal cellular and viral homologs. Mol. Cell. Biol 4, 1647–1652. [PubMed: 6092927]

Vargiu P, De Abajo R, Garcia-Ranea JA, Valencia A, Santisteban P, Crespo P, and Bernal J. (2004). The small GTP-binding protein, Rhes, regulates signal transduction from G protein-coupled receptors. Oncogene 23, 559–568. [PubMed: 14724584]

Vetter IR (2017). Interface analysis of small GTP binding protein complexes suggests preferred membrane orientations. Biol. Chem 398, 637–651. [PubMed: 28002022]

Volodko N, Gordon M, Salla M, Ghazaleh HA, and Baksh S. (2014). RASSF tumor suppressor gene family: biological functions and regulation. FEBS Lett. 588, 2671–2684. [PubMed: 24607545]

Vranken WF, Boucher W, Stevens TJ, Fogh RH, Pajon A, Llinas M, Ulrich EL, Markley JL, Ionides J, and Laue ED (2005). The CCPN data model for NMR spectroscopy: development of a software pipeline. Proteins 59, 687–696. [PubMed: 15815974]

Whitehead RH, Macrae FA, St John DJ, and Ma J. (1985). A colon cancer cell line (LIM1215) derived from a patient with inherited nonpolyposis colorectal cancer. J. Natl. Cancer Inst 74, 759–765. [PubMed: 3857372]

Wielaender F, Sarviaho R, James F, Hytönen MK, Cortez MA, Kluger G, Koskinen LL, Arumilli M, Kornberg M, Bathen-Noethen A, et al. (2017). Generalized myoclonic epilepsy with photosensitivity in juvenile dogs caused by a defective DIRAS family GTPase 1. Proc. Natl. Acad. Sci. USA 114, 2669–2674. [PubMed: 28223533]

Yang MH, Nickerson S, Kim ET, Liot C, Laurent G, Spang R, Philips MR, Shan Y, Shaw DE, Bar-Sagi D, et al. (2012). Regulation of RAS oncogenicity by acetylation. Proc. Natl. Acad. Sci. USA 109, 10843–10848. [PubMed: 22711838]

Zhang T, Inesta-Vaquera F, Niepel M, Zhang J, Ficarro SB, Machleidt T, Xie T, Marto JA, Kim N, Sim T, et al. (2012). Discovery of potent and selective covalent inhibitors of JNK. Chem. Biol 19, 140–154. [PubMed: 22284361]

Highlights

- Small GTPases undergo autophosphorylation through active site Ser/Thr substitution
- K-RAS autophosphorylation inhibits GTP hydrolysis and promotes nucleotide exchange
- K-RAS autophosphorylation promotes cellular transformation
- Autophosphorylation inhibits K-RAS binding to effectors

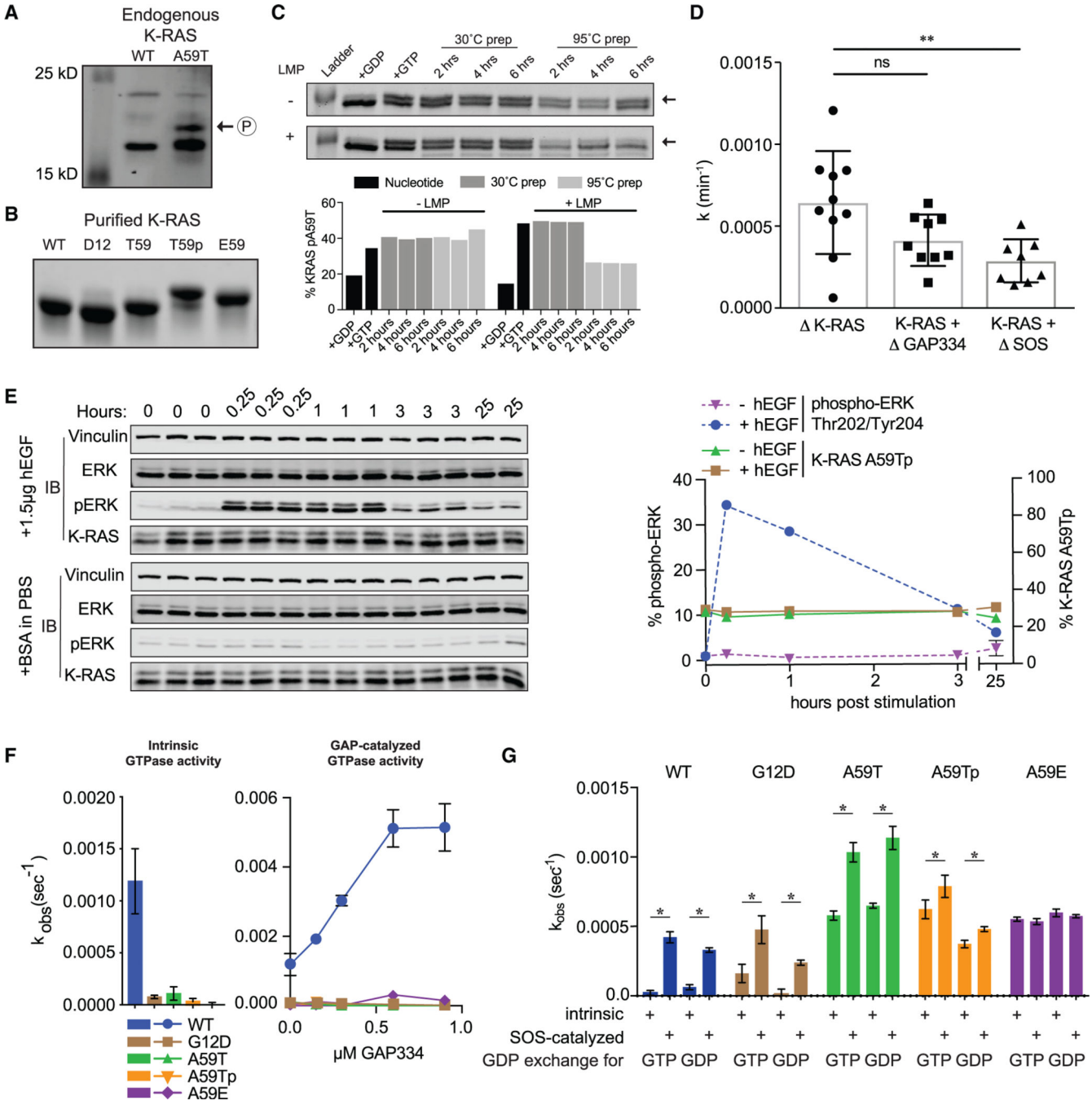

Figure 1. T59 phosphorylation alters K-RAS cycling

(A) Western blot of K-RAS in LIM1215 (WT) and SNU-175 (A59T) cells.

(B) SDS-PAGE of purified K-RAS with different residues at position 59.

(C) K-RAS^{A59T} incubated in the presence of GDP (lane 2) or GTP (lane 3). Dephosphorylation of K-RAS^{A59T} incubated with GTP with or without lambda phosphatase (LMP) for different times at 30°C after pre-incubation of protein at 30°C (lanes 4–6) or 95°C (lanes 7–9). Band quantification is shown below.

(D) Summary of K-RAS^{A59T} autophosphorylation kinetics alone or with regulatory proteins. Autophosphorylation rate constants (k) were calculated as v•[E0]$^{-1}$.
(E) Serum-starved and hEGF-stimulated SNU-175 cells showing phosphorylated ERK1/2 (pERK) or K-RAS. Replicates are labeled above the gel. Band quantification was normalized to the average “0” replicate and is shown on the right.
(F) Intrinsic and GAP-catalyzed hydrolysis (k) for K-RAS and mutants. Each bar or data point represents the average k (n = 3–4).
(G) Exchange of GDP-loaded K-RAS4B for mant-GTP or mant-GDP (n = 3–4).
* denotes $p < 0.05$ and ** denotes $p < 0.005$ by Student’s t test. Error bars represent ± SD.

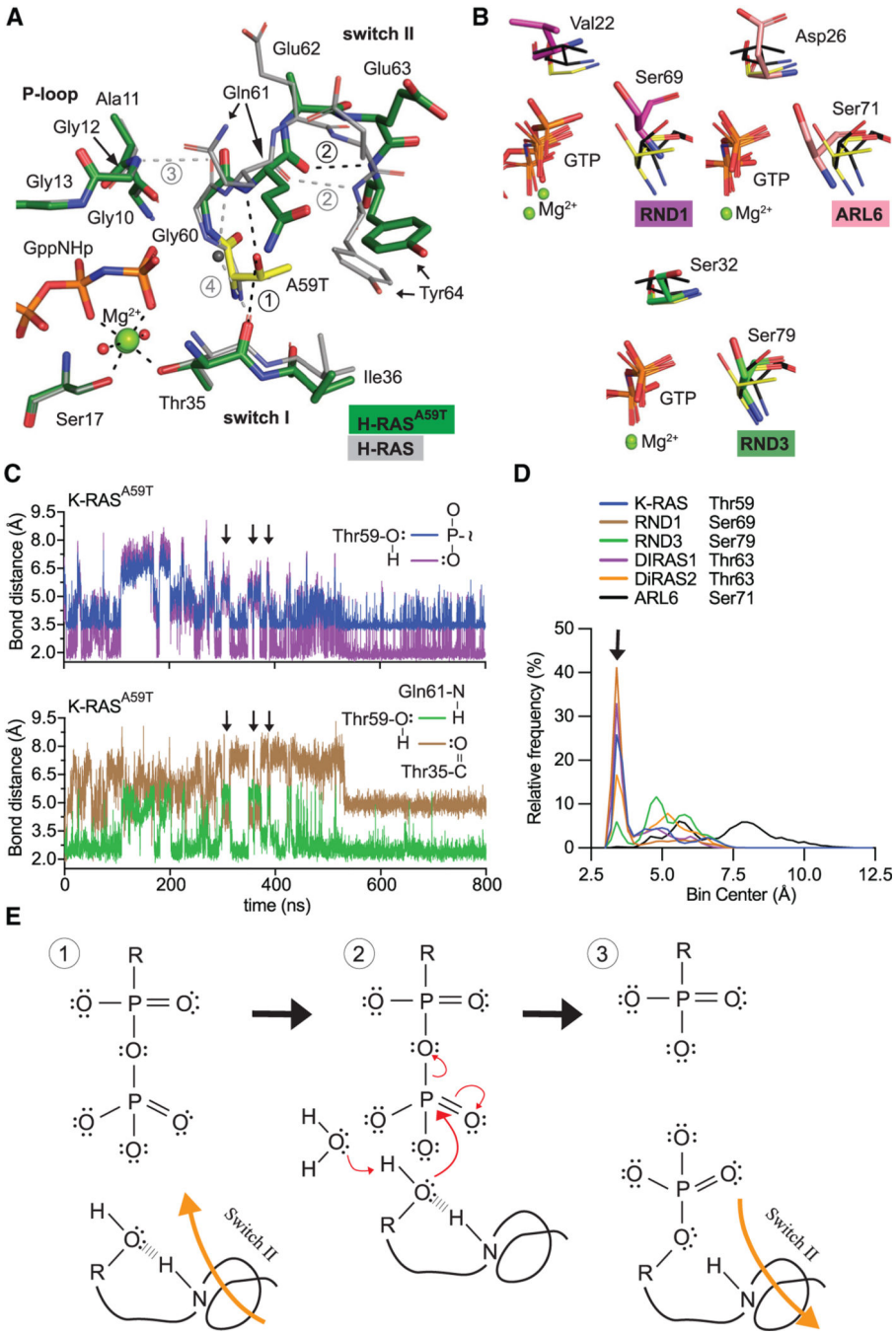

Figure 2. Conserved mechanism of autophosphorylation in GTPases

(A) Active site comparison of H-RAS^{A59T} crystal 1 (green) and WT H-RAS (PDB: 3K8Y, gray). Black and gray dashed lines are H-bonds made in H-RAS^{A59T} and WT structures. Thr59 is shown in yellow.

(B) Active site similarities between H-RAS^{A59T} and other small GTPases. Black sticks are from the H-RAS$^{G12V/A59T}$ structure (PDB: 521P) with an alternate Thr59 orientation.

(C) Bond distances made during simulation of K-RAS^{A59T} bound to GTP. Inset on the right shows measured bonds.

(D) Frequency distribution of nucleophile to γ-phosphate distances from MD simulations. (E) Proposed mechanism of autophosphorylation. The N-H group of switch II represents the backbone carbonyl of Gln61.

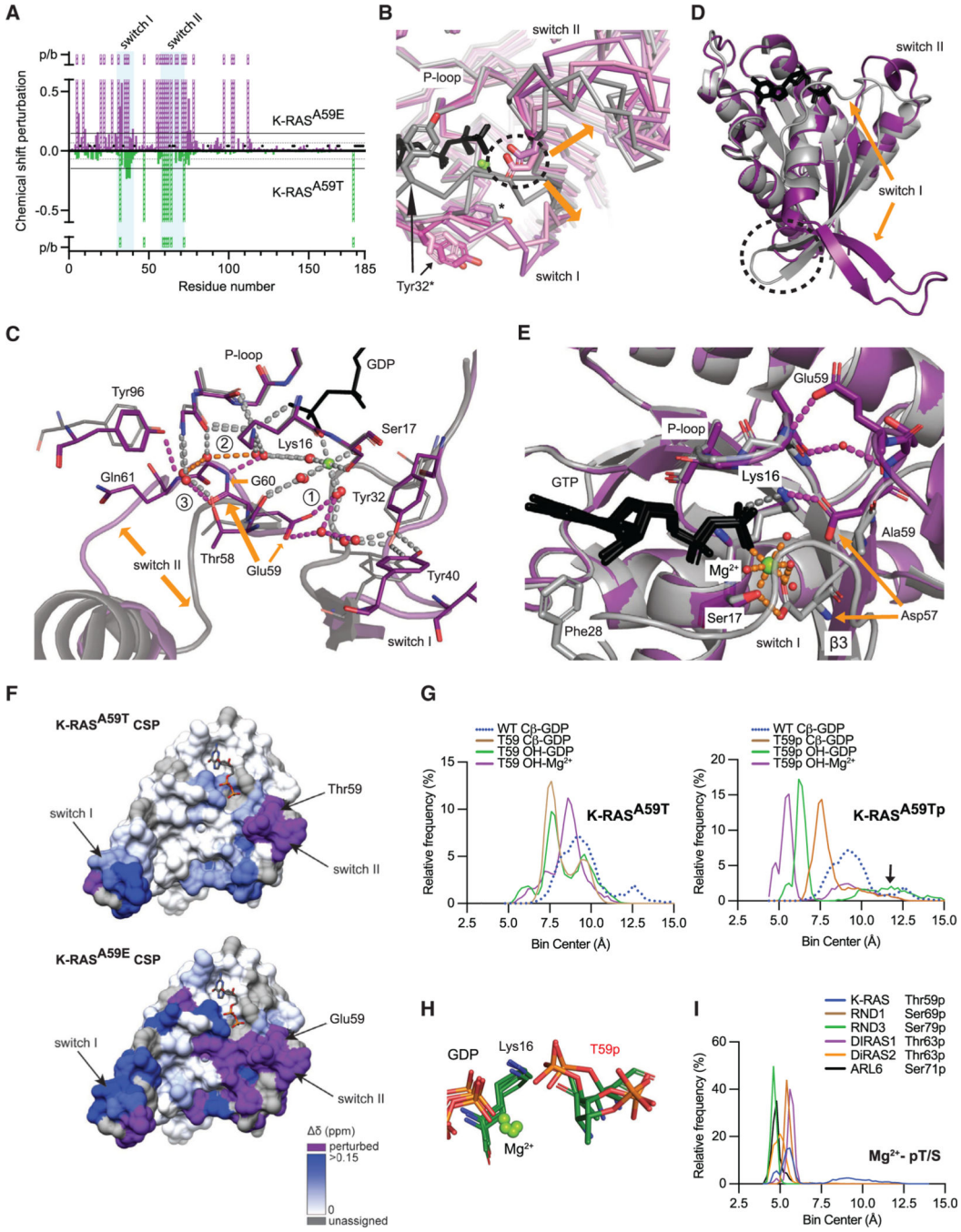

Figure 3. The molecular mechanism of hyperexchange

(A) Chemical shift perturbations induced by mutation of Ala59 plotted by K-RAS residue. 1H-15N cross-peaks for K-RAS^{A59E} or K-RAS^{A59T} are referenced to WT K-RAS-GppNHp. K-RAS^{A59T} versus WT chemical shift perturbations are shown as negative values to compare changes to K-RAS^{A59E}. Resonances detected in WT, but not in mutants, due to perturbations or severe peak broadening (p/b), are shown as dashed bars with an arbitrary value of 1 ppm. Residues not assigned for WT are marked with X. Horizontal lines show

threshold of mean chemical perturbation plus one SD for K-RAS^{A59T} (gray, dashed) and K-RAS^{A59E} (solid black).

(B) Comparison of K-RAS^{A59E} crystal structures bound to GppNHp (purple) and GDP (pink) to WT H-RAS bound to GDP or GppNHp (gray). Dashed circle indicates Glu59.

(C) Molecule B of H-RAS^{A59E} bound to GDP (purple). Glu59 rearranges the active site to favor GDP release, unlike the WT reference structure (PDB: 4OBE, gray). Gray dashes are shared H-bonds between structures. Colored dashes are described in text.

(D) Structure of GDP-bound K-RAS^{A59E} lacking Mg^{2+} compared to the WT reference structure. Dashed circle shows junction between switch I and helix 1.

(E) Glu59 and Asp57 stabilize a pro-exchange active site in K-RAS^{A59E}.

(F) Chemical shift perturbations (A) were mapped to the K-RAS surface. Color intensity represents magnitude of chemical shift changes relative to WT as defined by the scale. Resonances detected in WT, but not in the mutants, due to perturbation or broadening are shown in purple. Residues without assignments are colored in gray.

(G) Frequency distribution of bond distances during MD simulations of K-RAS^{A59T} and K-RAS^{T59p} bound to GDP.

(H) Cluster analysis of K-RAS^{T59p} MD simulation.

(I) Frequency distribution of bond distances during MD simulations of phosphorylated GTPases bound to GDP.

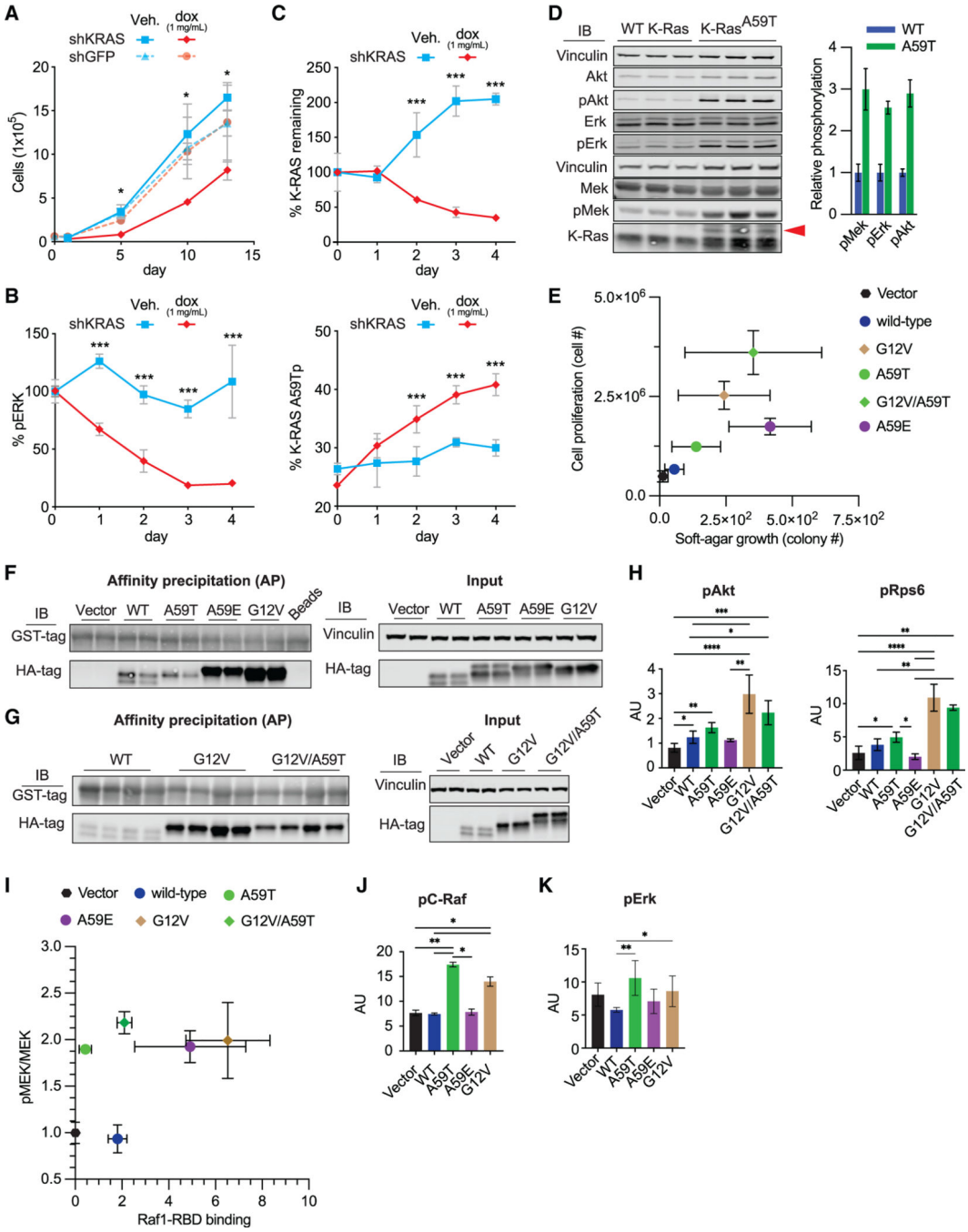

Figure 4. Roles of K-RAS^{A59T} and K-RAS^{A59E} in cellular transformation

(A) Effect of *KRAS* shRNA on proliferation in SNU-175 cells (n = 2–3).

(B) Effect of *KRAS* shRNA on ERK1/2 phosphorylation in SNU-175 cells (n = 2–3). Data are normalized to the average ERK1/2 phosphorylation on day 0.

(C) Effect of *KRAS* shRNA on K-RAS expression and autophosphorylation in SNU-175 cells (n = 2–3). Data are normalized to the average K-RAS expression on day 0 (upper).

(D) Baseline phosphorylation of Mek, Erk, and Akt in WT and K-Ras^{A59T} mouse embryonic stem cells after 6 h of serum starvation. The red arrow denotes

autophosphorylated K-RAS. Quantification is shown on the right and normalized to average phosphorylation for WT cells.

(E) Growth of NIH3t3 cells with ectopic K-RAS on plastic (x axis, n = 4–5) and in soft agar (y axis, n = 3) in 10% serum.

(F and G) Representative western blots from precipitation of GTP-bound K-RAS from NIH3t3 cells (F and G) by C-RAF-RBD-GST. Note that the upper band representing K-RAS^{T59p} is absent.

(H) Quantification of Akt (Ser473) and Rps6 (Ser235/236) phosphorylation (n = 4).

(I) Comparison of Mek phosphorylation (x axis, n = 4) and K-RAS-GTP (y axis, n = 4). Phosphorylated was normalized to total Mek. K-RAS-GTP was scaled to protein input and normalized to the average in cells expressing WT K-RAS.

(J) Quantification of C-Raf phosphorylation on Ser289/296/301 (n = 4).

(K) Quantification of Erk1/2 phosphorylation on Thr202/Tyr204 (n = 4).

In (A–C), errors bars represent ± SD and statistical analyses used Student's t test. For (H–K), errors bars represent ± SD and statistical analyses were performed with Mann-Whitney test. *, **, and *** represent P values of < 0.05, < 0.005, and < 0.0005, respectively. In (E–K), statistical comparisons and representative western blots are in Figure S4.

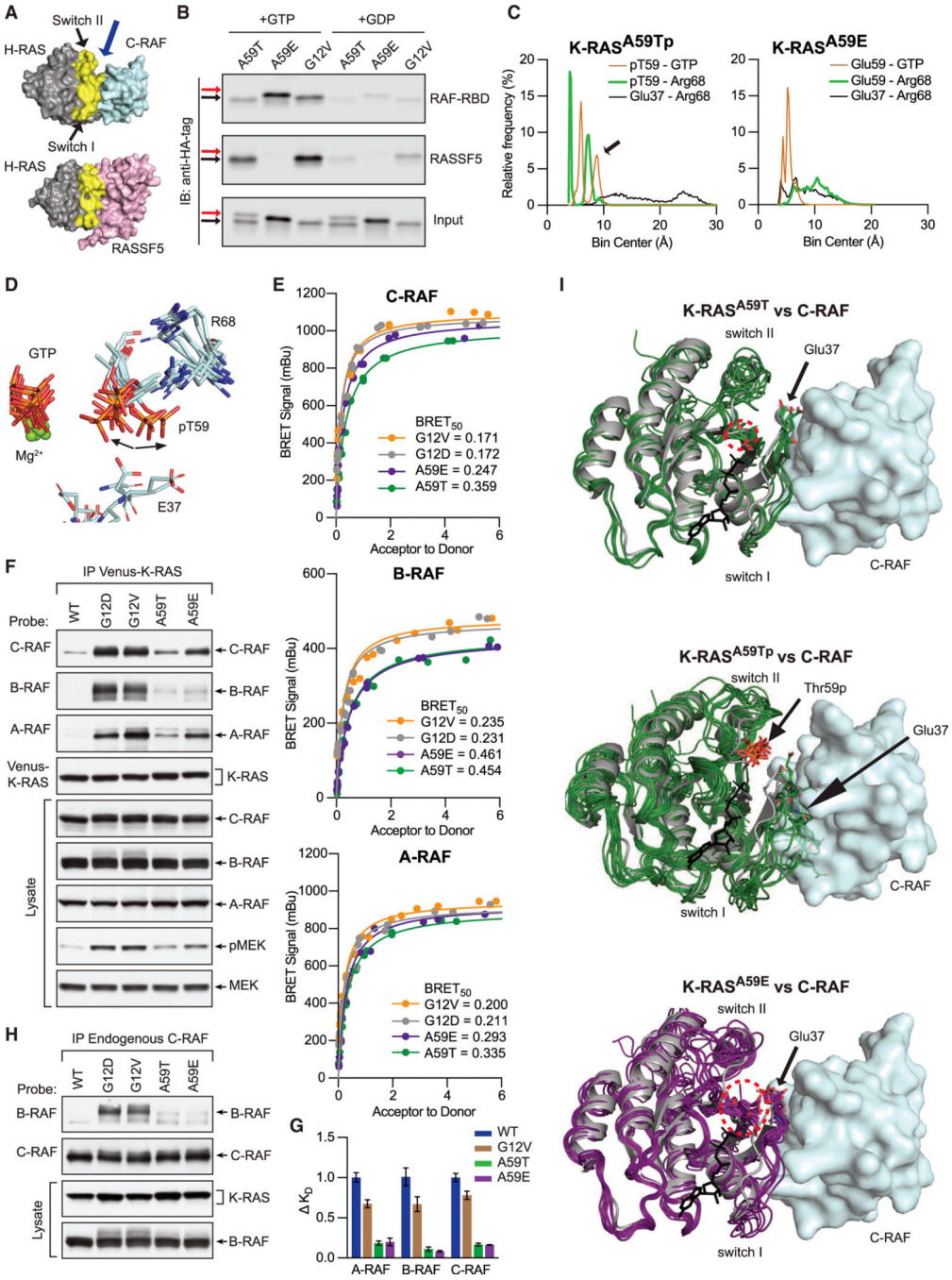

Figure 5. GTP induces phosphoryl movement to discriminate effector interactions

(A) Binding interfaces of C-RAF-RBD (PDB: 4G0N) and RASSF5-RBD (PDB: 3DDC). Blue arrows indicate Ala59 of RAS.

(B) Pull-down of ectopic K-RAS, preloaded with GTP or GDP, by C-RAF-RBD-GST or RASSF5-GST. Arrows denote non-phosphorylated (black) and phosphorylated (or A59E) (red) K-RAS.

(C) Frequency distribution of bond distances during MD simulations of mutant K-RAS bound to GTP.

(D) MD simulation cluster analysis of K-RAS^{T59p}.

(E) BRET saturation curves showing interaction between RAF isoform regulatory domains and K-RAS mutants in HEK293FT cells.

(F) Western blot of RAF isoforms co-immunoprecipitating with Venus-tagged K-RAS from serum-starved HeLa cells.

(G) Affinity changes of K-RAS for the RAF-RBDs determined by BLI. Data normalized to WT K-RAS (K_D^{WT}/K_D^{Mut}). Error bars represent ± SD (n = 2–4)

(H) Co-immunoprecipitation of B-RAF by C-RAF with different K-RAS mutants from serum-starved HeLa cells.

(I) Comparison of K-RAS conformations (green, purple) generated by cluster analysis of MD simulations to H-RAS (gray) bound to C-RAF (PDB: 4G0N, cyan). Nucleotide is shown in black.

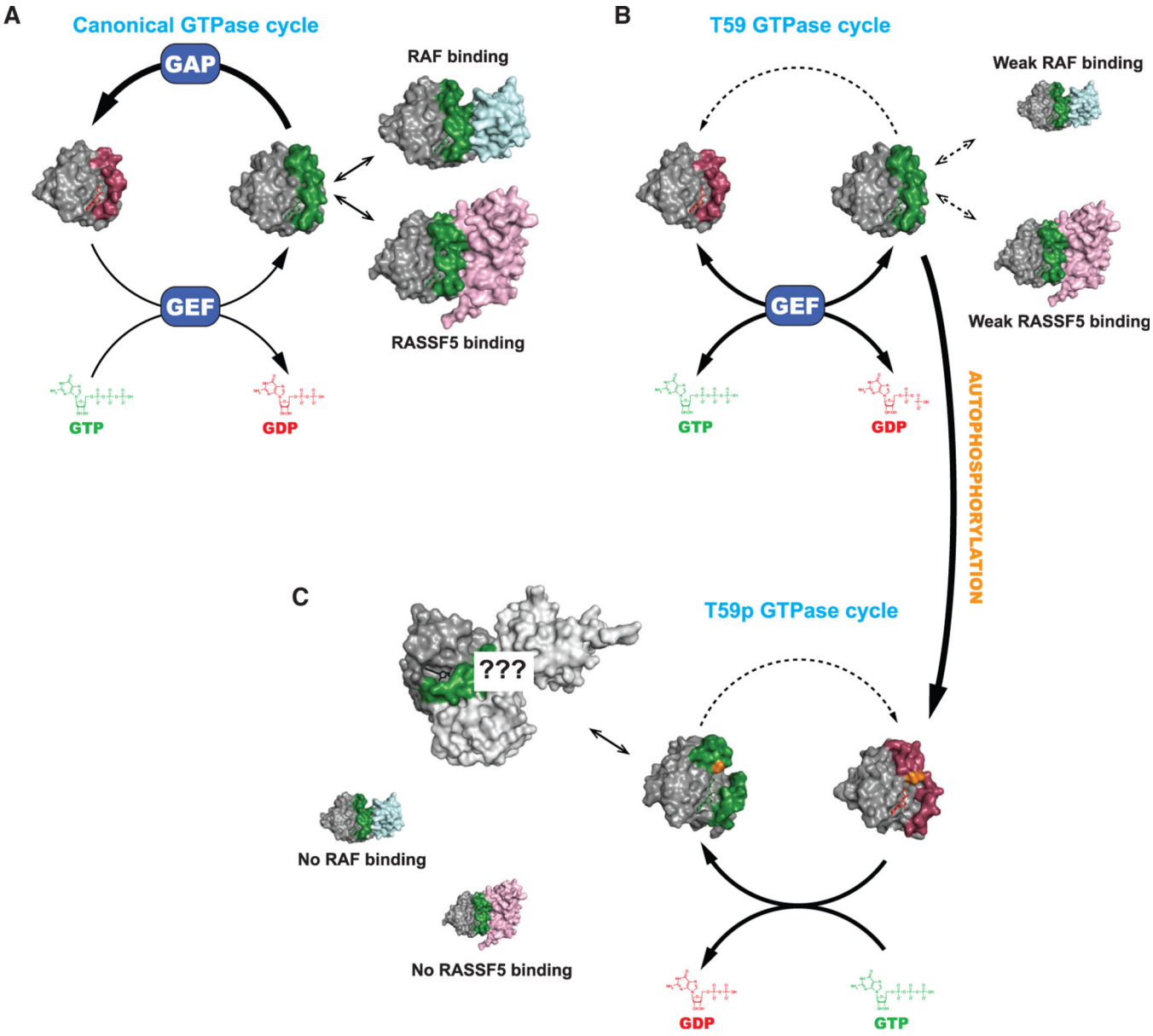

Figure 6. Influence of autophosphorylation on nucleotide cycling and effector engagement

(A) The normal GTPase cycle of K-RAS.

(B) Thr59 inhibits nucleotide hydrolysis and promotes intrinsic nucleotide exchange, activating K-RAS. Subsequently, the mutant shows weak binding to RAF and RASSF5 proteins.

(C) When Thr59 becomes phosphorylated (orange), K-RAS enters an alternative cycle where it becomes insensitive to GEF and loses the ability to bind to RAF and RASSF5 but opens up the possibility of interacting with novel effectors.

Table 1.

Small GTPases with autophosphorylation motif

Subfamily	GTPase	Switch II (G3 motif)	PDB	Biochemical features	Biological and disease associations	Cancer associated mutations[a]
RAS	K-RAS A59T	LDTTGQEEYSAM RDQYMRTG	-	High-exchange activity, low-GTPase activity, predominantly GTP-bound	Oncogene	Numerous
RAS	RASD1	LDTSGNHPFPA xxRLSILTG	-	Not studied	Circadian clock synchronization with light-dark cycles, neurogenesis, steroid response, tumor suppression, adipogenesis[b]	S80P Ewing Sarcoma
RAS	RASD2	LDTSGNHPFPA MRRLSILTG	-	Predominantly GTP-bound[c]	Huntington disease, Parkinson's disease, neurological function, mitophagy[d]	S71Y Breast
RAS	DIRAS1	TDTTGSHQFPAM QRLSISKG	2GF0	High-exchange activity, low-GTPase activity, predominantly GTP-bound, GAP-sensitive[e]	Tumor suppression, Autophagy, Epilepsy[f]	-
RAS	DIRAS2	TDTTGSHQFPAM QRLSISKG	2ERX	Low-GTPase activity, predominantly GTP-bound, GAP-sensitive[g]	Attention Deficit Hyperactive Disorder (ADHD), Tumor suppression, Autophagy[h]	T63M Colon and Stomach
RAB	RAB40A	WDTSGQGRFCT IFRSYSRGA	-	Not studied	Protein ubiquitination, cell deadhesion[i]	S71del Lung
RAB	RAB40B	WDxSGQGRFCTI FRSYSRGA	-	Not studied	Regulation of invadopodia, Gastric cancer[j]	-
RAB	RAB40C*	WDTSGQGRFCT IFRSYSRxA	-	Hydrolysis and GAP-sensitivity conserved[k]	Protein ubiquitination, noncanonical WNT-signaling, endocytosis, lipid droplet homeostasis[l]	-
RHO	RND1	WDTSGSPYYDN VRPLCYSDS	2CLS	Lacks intrinsic GTPase activity, has increased nucleotide exchange in favor of GTP[m]	Cell motility, smooth muscle contractility, Neurogenesis, Tumor suppression[n]	
RHO	RND2	WDTSGSxYYDN VRPLAYPDS	-	Not studied	Neurogenesis[o]	S63del Cervix
RHO	RND3	WDTSGSPYYDNV RPLSYPDS	1M7B	Lacks intrinsic GTPase activity and GAP-resistant[p]	Cell motility, smooth muscle contractility, Neurogenesis, Tumor suppression and cell cycle inhibition, oncogene[q]	-
ARF	ARL6	FDMSGQGxYRXL WEHYYKxx	2H57	Predominantly GDP bound[r]	Ciliopathies, Bardet-Biedl syndrome, BBSome regulation[s]	-

*Consensus sequence was generated by an 85% similarity cutoff, instead of a 95% cutoff for all others.

[a]Tate et al., 2019.

[b]Bouchard-Cannon et al., 2018; Cha et al., 2013; Cheng et al., 2004; Kemppainen and Behrend, 1998; Tang et al., 2019.

[c] Vargiu et al., 2004.

[d] Ghiglieri et al., 2015; Napolitano et al., 2018; Shahani et al., 2016; Sharma et al., 2019; Swarnkar et al., 2015.

[e] Gasper et al., 2010; Kontani et al., 2002.

[f] Bergom et al., 2016; Sutton et al., 2018; Wielaender et al., 2017.

[g] Gasper et al., 2010; Kontani et al., 2002; Ogita et al., 2015.

[h] Reif et al., 2011; Sutton et al., 2018.

[i] Dart et al., 2015.

[j] Jacob et al., 2016; Li et al., 2015.

[k] Luo et al., 2017.

[l] Lee et al., 2007; Luo et al., 2017; Rodriguez-Gabin et al., 2004.

[m] Nobes et al., 1998.

[n] Mouly et al., 2019; Okada et al., 2015; Riou et al., 2010.

[o] Heng et al., 2008; Riou et al., 2010.

[p] Foster et al., 1996.

[q] Paysan et al., 2016; Riou et al., 2010.

[r] Kobayashi et al., 2009.

[s] Fan et al., 2004; Nachury, 2018.

Table 2.

Data collection and structure refinement statistics

PDB ID	H-RAS A59T GppNHp crystal 1 7JIF	H-RAS A59T GppNHp crystal 2 7JIG	H-RAS A59E GppNHp 7JIH	H-RAS A59E GDP 7JII	K-RAS A59E GDP 7KMR
Data collection and processing					
Resolution range	33.49–1.757 (1.82–1.757)	33.74–2.322 (2.405–2.322)	29.17–1.989 (2.06–1.989)	36.14–1.532 (1.587–1.532)	55.57–1.51 (1.564–1.51)
Space group	$P3_221$	$P3_221$	$P12_11$	P1	P321
Unit cell dimensions					
a, b, c (Å)	39.567 39.567 158.302	38.964 38.964 159.048	55.675 49.832 57.32	38.593 37.946 56.254	78.4 78.4 55.57
α, β, γ (°)	90 90 120	90 90 120	90 117.812 90	107.362 107.185 95.319	90 90 120
Total reflections	45757	41434	50242	60862	311129
Unique reflections	15450	6642	19261	43101	31274
Multiplicity	4.3	6.5	3.3	2.2	9.9 (10.4)
completeness (%)	69.07 (7.99)	94.04 (61.02)	80.00 (9.58)	65.82 (6.14)	99.91 (99.93)
I/sigma(I)	29.0 (1.9)	9.5 (1.5)	6.6 (0.5)	38.3 (9.2)	14.39 (1.22)
Wilson B-factor	24.6	29.12	33.07	16.83	20.83
R_{merge}	0.032	0.076	0.083	0.02	0.158
R_{meas}	0.036	0.082	0.098	0.028	0.167
R_{pim}	0.016	0.031	0.051	0.018	0.054
CC1/2	(1)	(0.765)	(0.597)	(0.952)	(0.998)
CC*	(1)	(0.931)	(0.865)	(0.988)	(0.999)
Crystal structure refinement					
Used reflections	10481 (119)	6204 (393)	15420 (182)	28213 (263)	31274 (3066)
Reflections R_{free}	1047 (11)	611 (43)	1575 (22)	2005 (16)	1542 (168)
R_{work}	0.1708 (0.4107)	0.1807 (0.2688)	0.1960 (0.3317)	0.1577 (0.2410)	0.1615 (0.2452)
R_{free}	0.2456 (0.6982)	0.2625 (0.3255)	0.2553 (0.3940)	0.2021 (0.2879)	0.1967 (0.2950)
Atom information					
macromolecules	1339	1294	2425	2640	1357

PDB ID	H-RAS A59T GppNHp crystal 1 7JIF	H-RAS A59T GppNHp crystal 2 7JIG	H-RAS A59E GppNHp 7JIH	H-RAS A59E GDP 7JII	K-RAS A59E GDP 7KMR
ligands	39	33	78	62	28
solvent	155	61	102	336	136
Protein residues	168	168	322	336	172
RMS (bonds, Å)	0.007	0.007	0.008	0.007	0.013
RMS (°)	1.21	1.19	1.29	1.23	2.03
Ramachandran (%)					
favored	98.78	95.12	96.73	97.56	98.2
allowed	1.22	4.27	2.94	2.13	1.8
outliers	0	0.61	0.33	0.3	0.0
Clashscore	4.77	6.56	4.71	4.16	0.0
B-factors					
Average	23.26	30.85	35.24	21.06	28.99
macromolecules	22.74	30.89	35.32	20.39	28.16
ligands	20.45	26.19	33.74	17.14	20.97
solvent	28.40	32.58	34.57	27.06	38.87

Parentheses represent highest resolution averages.

KEY RESOURCES TABLE

REAGENT or RESOURCE	SOURCE	IDENTIFIER
Antibodies		
A-RAF	Santa Cruz	Cat#: sc-408; RRID: AB_630882
AKT (pan) (40D4)	Cell Signaling Technologies	Cat#: 2920; RRID:AB_1147620
Anti-GFP	MBL International	Cat#:D153–3; RRID:AB_591817
Anti-GST (91G1)	Cell Signaling Technologies	Cat#: 2625; RRID:AB_490796
Anti-HA-tag (6E2)	Cell Signaling Technologies	Cat#: 2367; RRID:AB_10691311
Anti-Venus	Roche	Cat#: 118114460001
B-RAF	Santa Cruz	Cat#: sc-5284; RRID:AB_2721130
C-RAF	BD Pharmagen	Cat#: 610152; RRID:AB_397553
c-RAF (D5X6R) Mouse mAb	Cell Signaling Technologies	Cat#: 12552S; RRID:AB_2728706
Goat anti-Mouse IgG (H+L) Highly Cross-Adsorbed Secondary Antibody, Alexa Fluor 680	Invitrogen	Cat#: A-21058; RRID:AB_2535724
Goat anti-Rabbit IgG (H+L) Highly Cross-Adsorbed Secondary Antibody, Alexa Fluor Plus 800	Invitrogen	Cat#: A-32735; RRID:AB_2633284
MEK1	BD Biosciences	Cat#: 610122; RRID:AB_397528
MEK1/2 (L38C12)	Cell Signaling Technologies	Cat#: 4694; RRID:AB_10695868
p44/42 MAPK (ERK1/2) (L34F12)	Cell Signaling Technologies	Cat#: 4696; RRID:AB_390780
pC-RAF (s289/296/301)	Cell Signaling Technologies	Cat#: 9431; RRID:AB_561402
Phospho-Akt (Ser473) (D9E) XP®	Cell Signaling Technologies	Cat#: 4060; RRID:AB_2315049
Phospho-MEK1/2 (Ser217/221)	Cell Signaling Technologies	Cat#: 9121; RRID:AB_331648
Phospho-MEK1/2 (Ser217/221) (41G9)	Cell Signaling Technologies	Cat#: 9154; RRID:AB_2138017
Phospho-p44/42 MAPK (ERK1/2) (Thr202/ Tyr204) (197G2)	Cell Signaling Technologies	Cat#: 4377; RRID:AB_331775
Phospho-S6 Ribosomal Protein (Ser235/236)	Cell Signaling Technologies	Cat#: 2211; RRID:AB_331679
polyclonal KRAS antibody	Proteintech	Cat#: 12063–1-AP; RRID:AB_878040
RAS10	Millipore-Sigma	Cat#: 05–516; AB_2121151
S6 Ribosomal Protein (54D2)	Cell Signaling Technologies	Cat#: 2317; RRID:AB_2238583
Vinculin (E1E9V) XP®	Cell Signaling Technologies	Cat#: 13901; RRID:AB_2728768
Bacterial and virus strains		
BL21 (DE3 Codon$^+$)	Agilent	Cat#: 230280
BL21 (DE3)	Thermo Scientific	Cat#: C600003
BL21-A1	Thermo Fisher Scientific	Cat#: C607003
DH5α-T1R	Invitrogen	Cat#: 12297–016
pCL-Eco	Addgene	Cat#: 12371
Tet-pLKO-puro shKRAS	Addgene	Cat#: 116871
TOP10 *E. coli* strain	Fisher Scientific	Cat#: C404003
Chemicals, peptides, and recombinant proteins		
1.0 M Calcium acetate hydrate	Hampton Research	Cat#: HR2–567
1.0 M HEPES pH 7.5	Hampton Research	Cat#: HR2–729

REAGENT or RESOURCE	SOURCE	IDENTIFIER
1.0 M Magnesium acetate tetrahydrate	Hampton Research	Cat#: HR2–561
100% glycerol	Hampton Research	Cat#: HR2–623
100% PEG400	Hampton Research	Cat#: HR2–603
100X Glutamax supplement	Thermo Fisher Scientific	Cat#: 35050061
100X MEM Non-Essential Amino Acids Solution	Life Technologies	Cat#: 11140–050
10X CutSmart buffer	New England Biolabs	Cat#: R3195T
1X Knockout DMEM	Life Technologies	Cat#: 10829–018
2-Mercaptoethanol	Millipore-Sigma	Cat#: M3148–250ML
2’/3′-O-(N-Methyl-anthraniloyl)-guanosine-5′-diphosphate	Fisher Scientific	Cat#: M12414
2’/3′-O-(N-Methyl-anthraniloyl)-guanosine-5′-triphosphate	Fisher Scientific	Cat#: M12415
4.0 M Magnesium chloride hexahydrate	Hampton Research	Cat#: HR2–803
5.0 M Sodium chloride	Hampton Research	Cat#: HR2–637
50% PEG3350 mono disperse	Hampton Research	Cat#: HR2–527
5X Phusion HF Buffer	New England Biolabs	Cat#: M0530S
Accucore C18 resin	ThermoFisher Scientific	N/A
Antibiotic Antimycotic Solution (PenStrep)	Sigma-Aldrich	Cat#: A5955
Chymotrypsin	Promega	Cat #V106A
Coelenterazine-h	N/A	N/A
Deoxynucleotide (dNTP) Solution Mix	New England Biolabs	Cat#: N0447S
DMSO	Sigma-Aldrich	Cat#: D2650–100mL
Dulbeccos Modification of Eagles Medium (DMEM)	TC-Corning	Cat#: 10–013-CV
EcoRV-HF® restriction enzyme	New England Biolabs	Cat#: R3195T
ESGRO ®Leukemia Inhibitory Factor (LIF), 1 million units/1mL	Millipore-Sigma	Cat#: ESG1106
Fetal Bovine Serum (FBS)	GE Healthcare	Cat#: SH30070.03
Gelatin from bovine skin	Sigma-Aldrich	Cat#: G9391–100G
GreenGlo™ Safe DNA Dye, 20,000X in Water	Denville Scientific	Cat#: ca3600
Guanosine 5′-[β,γ-imido]triphosphate trisodium salt hydrate	Sigma-Aldrich	Cat#: G0635–100MG
HyClone Defined Fetal Bovine Serum (FBS), US Origin	Cytiva	Cat#: SH30070.03
Intercept ®(TBS) Blocking Buffer	LI-COR Biosciences	Cat#: 927–6003
Intercept ®T20 (TBS) Antibody Diluent	LI-COR Biosciences	Cat#: 927–65001
Iodoacetamide	ThermoFisher Scientific	Cat #A39271
Lambda Phosphatase	New England BioLabs	Cat#: P0753S
Modified Terrific Broth	Fisher Scientific	Cat#: BP9729–600
Phusion ®High-Fidelity DNA Polymerase	New England Biolabs	Cat#: M0530S
Radioimmunoprecipitation assay (RIPA) buffer	Boston Bioproducts	Cat#: BP-115–500
RPMI 1640	Fisher Scientific	Cat#: MT10040CV
Tris(2-carboxyethyl)phosphine	ThermoFisher Scientific	Cat #77720
0.05% Trypsin EDTA	Invitrogen	Cat#: 25300–120
UltraPure™ DNase/RNase-Free Distilled Water	Invitrogen	Cat#: 10977023
Critical commercial assays		

REAGENT or RESOURCE	SOURCE	IDENTIFIER
EnzChek™ Phosphate Assay Kit	Thermo Fisher Scientific	Cat#: E6646
Mouse ES Cell Nucleofector®Kit	Lonza	Cat#: VPH-1001
PureLink® HiPure Plasmid Filter Maxiprep kit	Thermo Fisher Scientific	Cat#: K2100–17
Quick-DNA 96 kit	Zymo Research	Cat#: D3012
QuikChange site-directed mutagenesis	Agilent	Cat#: 200519
XtremeGENE9 transfection Kit	Millipore-Sigma	Cat#: 6365779001
Deposited data		
H-RAS A59E GDP	https://www.rcsb.org	PDB: 7JII
H-RAS A59T GppNHp crystal 1	https://www.rcsb.org	PDB: 7JIF
H-RAS A59T GppNHp crystal 2	https://www.rcsb.org	PDB: 7JIG
H-RAS A59E GppNHp	https://www.rcsb.org	PDB: 7JIH
K-RAS A59E GDP	https://www.rcsb.org	PDB: 7KMR
Raw data western blot data from figures were deposited on Mendeley at https://dx.doi.org/10.17632/9n7bryshg3.1	https://data.mendeley.com	Mendeley data: https://doi.org/10.17632/9n7bryshg3.1
Experimental models: Cell lines		
EmbryoMax® Primary Mouse Embryonic Fibroblasts	Millipore-Sigma	Cat#: PMEF-CFX
HEK293FT cells	Thermo Fisher Scientific	Cat#: R70007; RRID: CVCL_6911
HEK293t cells	ATCC	Cat#: CRL-3216; RRID: CVCL_0063
HeLa cells	ATCC	Cat#: CCL-2; RRID: CVCL_0030
LIM1215 cells	Whitehead et al., 1985	N/A; RRID: CVCL_2574
K-Ras(+/LSL-wildtype) Mouse Embryonic Stem cells	Poulin et al., 2019	N/A
K-Ras(A59T/LSL-A59T) Mouse Embryonic Stem cells	This study	N/A
NIH 3T3 cells	ATCC	Cat#: CRL-1658; RRID: CVCL_0594
Oligonucleotides		
5′-CTTGGATATTCTC GACACAACAGGTCA AGAGGAGTACAG-3′	Integrated DNA Technologies	pBABE KRAS4B A59T Forward
5′-CTGTACTCCTCT TGACCTGTTGTGTCG AGAATATCCAAG-3′	Integrated DNA Technologies	pBABE KRAS4B A59T Reverse
5′-GGATATTCTCG ACACAGAAGGTCAA GAGGAGTACAG-3′	Integrated DNA Technologies	pBABE KRAS4B A59E Forward
5′-CTGTACTCCTCT TGACCTTCTGTGTCGA GAATATCC-3′	Integrated DNA Technologies	pBABE KRAS4B A59E Reverse
5′-GTAGTTGGAGC TGTTGGCGTA GGCAAG-3′	Integrated DNA Technologies	pBABE KRAS4B G12V Forward
5′-CTTGCCTACGC CAACAGCTCC AACTAC-3′	Integrated DNA Technologies	pBABE KRAS4B G12V Reverse
5′-GTGGTAGTTGGAGCTCGTGG CGTAGGCAAG-3′	Integrated DNA Technologies	pBABE KRAS4B G12R Forward
5′-CTTGCCTACGCCACGAGCTCCA ACTACCAC-3′	Integrated DNA Technologies	pBABE KRAS4B G12R Reverse
5′-GGTGGTTGGTGCCGATGGTG TGGGTAAAAG-3′	Integrated DNA Technologies	pET21 KRAS4B G12D Forward

REAGENT or RESOURCE	SOURCE	IDENTIFIER
5′-CTTTTACCCACACCATCGGCA CCAACCACC-3′	Integrated DNA Technologies	pET21 KRAS4B G12D Reverse
5′-CATTCTGGATACCACCGGCC AGGAAG-3′	Integrated DNA Technologies	pET21 KRAS4B A59T Forward
5′-CTTCCTGGCCGGTGGTAT CCAGAATG-3′	Integrated DNA Technologies	pET21 KRAS4B A59T Reverse
5′-GACATTCTGGATACCGAAGGC CAGGAAGAGTATAG-3′	Integrated DNA Technologies	pET21 KRAS4B A59E Forward
5′-CTATACTCTTCCTGGCCTTCGG TATCCAGAATGTC-3′	Integrated DNA Technologies	pET21 KRAS4B A59E Reverse
5′-CACCGTTCTCGACACAGCAGGT CAAG-3′	Integrated DNA Technologies	SaCas9 gRNA 1 Forward
5′-AAACCTTGACCTGCTGTGTC GAGAAC-3′	Integrated DNA Technologies	SaCas9 gRNA 1 Reverse
5′-TGTGACCATTAGCATTGT TTGC-3′	Integrated DNA Technologies	mES Ex2 genotyping Forward primer
5′-CTTAAACCCACCTATAAT GGTG-3′	Integrated DNA Technologies	mES Ex2 genotyping Reverse primer
5′-AGTAATTGATGGAGAAA CCTG-3′	Integrated DNA Technologies	mES Ex2 Sequencing Forward primer
5′-ATAATGGTGAATATCTT CAAA-3′	Integrated DNA Technologies	mES Ex2 Sequencing Reverse primer
5′-CTGTAATAAT CCAGACTGTG TTTCTCCCTT CTCAGGACTCC TACAGGAAAC AAGTAGTAAT TGATGGAGAA ACCTGTCTCT TGGATATCCT CGACACAACA GGTCAAGAAG AGTACAGTGC AATGAGGGAC CAGTACATGA GAACTGGGGA GGGCTTTCTT TGTGTATT TGCCATAAA TAATACTAA ATCATTTG AAGAT-3′	Integrated DNA Technologies	Repair template for CRISPR experiments
Recombinant DNA		
100 bp DNA ladder	New England Biolabs	Cat#: N3231L
6xHis-GAP (715–1047)	This study	N/A
6xHis-K-RAS4B	This study	N/A
6xHis-SOS11 (564–1049)	This study	N/A
Gateway pDEST15 vector	Thermo Scientific	Cat#: 11802014
H-RAS (1–166)	Buhrman et al., 2010	N/A
pBABE-hygro vector	Addgene	Cat#: 1765
pCMV5-Venus-K-Ras4B	Terrell et al., 2019	N/A
pET-21a(+) vector	EMD Biosciences	https://www.emdmillipore.com/US/en/product/pET-21+-DNA-Novagen,EMD_BIO-69770www.emdmillipore.com/US/en/product/pET-21+-DNA-Novagen,EMD_BIO-69770
pET28 vector	EMD Biosciences	https://www.emdmillipore.com/US/en/product/pET-28a+-DNA-Novagen,EMD_BIO-69864www.emdmillipore.com/US/en/product/pET-28a+-DNA-Novagen,EMD_BIO-69864
pGEX-4T2-A-RAF(17–94)	Smith and Ikura, 2014	N/A
pGEX-4T2-B-RAF(150–233)	Smith and Ikura, 2014	N/A
pGEX-4T2-C-RAF(53–137)	Fang et al., 2020	N/A

REAGENT or RESOURCE	SOURCE	IDENTIFIER
pGEX-4T2-RASSF5(199–367)	Smith and Ikura, 2014	N/A
pLHCX-WT-RafReg-Rluc8 (A-, B-, C-Raf)	Terrell et al., 2019	N/A
pX601-AAV-CMV::NLS-SaCas9-NLS-3xHA-bGHpA;U6::BsaI-sgRNA	Addgene	Cat#: 61591
Raf1-RBD	Addgene	Cat#: 13338
RAS pathway collection v2.0	Addgene	Kit#: 1000000070
RASSF1	Addgene	Cat#: 70535
RASSF10	Addgene	Cat#: 70537
RASSF2	Addgene	Cat#: 70539
RASSF3	Addgene	Cat#: 70541
RASSF4	Addgene	Cat#: 70543
RASSF5	Addgene	Cat#: 70545
RASSF6	Addgene	Cat#: 70547
RASSF7	Addgene	Cat#: 70549
RASSF8	Addgene	Cat#: 70551
RASSF9	Addgene	Cat#: 70553
Software and algorithms		
CHARM-GUI (solution builder)	Brooks et al., 2009; Jo et al., 2008; Lee et al., 2016	https://charmm-gui.org/?doc=input/solution
Chimera (ver. 1.15)	Pettersen et al., 2004	https://www.cgl.ucsf.edu/chimera/
Coot	Emsley and Cowtan, 2004	https://www2.mrc-lmb.cam.ac.uk/personal/pemsley/coot/
GraphPad (ver. 9.1.0)	Prism	https://www.graphpad.com
GROMACS (ver. 2020.1)	Abraham et al., 2015	http://www.gromacs.org
HKL3000 package	Otwinowski and Minor, 1997	https://hkl-xray.com/hkl-3000
Image Studio lite (ver. 5.2.5)	LI-COR	https://www.licor.com/bio/image-studio/
NMRPipe	Delaglio et al., 1995	https://groups.io/g/nmrpipe
CcpNmr	Vranken et al., 2005	N/A
PHENIX (ver. 1.11.1–2575)	Adams et al., 2010	https://phenix-online.org
PyMOL (ver. 2.4.0)	Schrodinger	https://pymol.org/2/
Sequest	Eng et al., 1994	http://fields.scripps.edu/yates/wp/?page_id=17
SnapGene (ver. 5.2.4)	GSL Biotech	N/A
VMD (ver. 1.9.4a38)	Humphrey et al., 1996	http://www.ks.uiuc.edu/Research/vmd/
XDS	Kabsch, 2010	https://xds.mr.mpg.de
Other		
96-Well Clear Bottom Black or White Polystyrene Microplates	Corning	Cat#: 3917
96-well black-walled plate (OptiPlate)	Perkin Elmer	Cat#: 6005270
384-well white-walled plate (CulturePlate)	Perkin Elmer	Cat#: 6007680
Accela600 liquid chromatography pump	Thermo Fisher Scientific	N/A

REAGENT or RESOURCE	SOURCE	IDENTIFIER
AKTA Pure	Cytiva	http://www.cytivalifesciences.com/en/us/shop/chromatography/chromatographysystems/akta-pure-p-05844
Cellometer ®AutoT4 cell counter	Nexcelom Bioscience	https://www.nexcelom.com/nexcelomproducts/automated-cell-counters/cellometer-auto-t4-automated-cellcounter/
ChemiDoc XRS+ System	Bio-Rad	Cat#: 1708265
Epson Perfection V600 Photo Scanner	Epson	Cat#: B11B198011
Famos Autosampler	LC Packings	N/A
HiTrap QHP column	Cytiva	Cat#: 17115401
HiTrap TALON column	Cytiva	Cat#:29048565
MicroMax007HF	Rigaku	N/A
Mono-Q column	Cytiva	Cat#: 17516601
NEO III HD 800MHz spectrometer	Bruker	N/A
Ni-NTA beads	QIAGEN	Cat#: 30210
NT8 Crystallization robot	Formulatrix	https://formulatrix.com/proteincrystallization-systems/nt8crystallization-robot/
Nucleofector® II Device	Lonza	N/A
Octet RED-384 biolayer interferometry biosensor instrument	Sartorius	https://www.sartorius.com/en/products/protein-analysis/octet-label-freedetection-systems
Odyssey ®CLx	LI-COR	https://www.licor.com/documents/8prh6ps2abjbemx68412
PD-10 desalting column	Cytiva	Cat#: 17085101
PHERAstar *Plus* plate reader	BMG Labtech	https://www.bmglabtech.com/pherastardetection-system/
Phoenix liquid handler	ArtRobbins	https://www.artrobbins.com/crystalphoenix
Protein G Sepharose	Cytiva	Cat#: GE17–0618-01
Q Exactive mass spectrometer	Thermo Fisher Scientific	N/A
R-Axis IV^{2+}	Rigaku	N/A
RockImager Protein Crystallization Imager	Formulatrix	https://formulatrix.com/proteincrystallization-systems/rock-imagercrystallization-imagers/
StageTip	N/A	N/A
Superdex 75 10/300 column	Cytiva	Cat#: 17517401
Synergy H1 Hybrid Multi-Mode Reader microplate	BioTek	https://www.biotek.com/products/detection-hybrid-technology-multi-modemicroplate-readers/synergy-h1-hybridmulti-mode-reader/
Tecan Infinite M1000 plate reader	Thermo Fisher Scientific	N/A
Ultra-15 Centrifugal Filter Units (10kDa MWCO)	Fisher Scientific	Cat#: UFC901008
Zeba™ Spin Desalting Columns	Thermo Fisher Scientific	Cat#: PI89892
Protein model: Wildtype H-RAS GppNHp	Buhrman et al., 2010	3K8Y
Protein model: Wildtype H-RAS GDP	Scheidig et al., 1999	1CTQ
Protein model: Wildtype H-RAS bound to GAP and AlF_x	Scheffzek et al., 1997	1WQ1
Protein model: H-RAS G12V/A59T bound to GTP	Krengel et al., 1990	521P
Protein model: RND3 bound to GTP	Fiegen et al., 2002	1M7B
Protein model: RND1 bound to GTP	N/A	2CLS
Protein model: DIRAS2 bound to GDP	N/A	2ERX

REAGENT or RESOURCE	SOURCE	IDENTIFIER
Protein model: DIRAS1 bound to GDP	N/A	2GF0
Protein model: ARL6 bound to GTP	Structural Genomics Consortium	2H57
Protein model: Wildtype K-RAS bound to GDP	Hunter et al., 2014	4OBE
Protein model: Wildtype H-RAS bound to the RBD domain of RASSF5	Stieglitz et al., 2008	3DDC
Protein model: Wildtype H-RAS bound to the RBD of C-RAF	Fetics et al., 2015	4G0N
Protein model: Wildtype H-RAS bound to the RBD-CRD of C-RAF	Cookis and Mattos, 2021	7JHP
Protein model: Wildtype K-RAS bound to the RBD-CRD of C-RAF	Tran et al., 2021	6XI7
Protein model: H-RAS G12V bound to the RBD of PI3K	Pacold et al., 2000	1HE8
Protein model: Wildtype K-RAS bound to the RBD-PH domain of SIN1	Castel et al., 2021	7LC1